Studies of Injection Seeding and Threshold in β-BaB_2O_4 Optical Parametric Oscillator

Philip Schlup

OCTOBER 1997

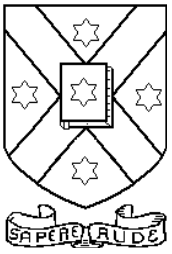

University of Otago

A dissertation submitted for the partial fulfilment of
the degree of Bachelor of Science with Honours

Acknowledgements

I should like to express my gratitude to all the people who have helped me on this project, especially to Iain McKinnie for his endless enthusiasm, humour and outstanding supervision, to Stuart Butterworth and Don Warrington for guidance at various times throughout the year, to Noah Russell and Piyush Jain for help on using the OPO, and to Andrew Tagg for proof-reading the dissertation.

Abstract

Injection seeding in a Type I (e → o + o) singly resonant collinear β-BaB_2O_4 optical parametric oscillator, pumped by the third harmonic of a *Q*-switched Nd:YAG laser, has been achieved at the idler wavelength. The seed source was a diode laser which was scanned over 19 GHz by an external cavity. The effects on threshold of changing output coupler, cavity length and pump spotsize have been measured and compared to a simple theoretical model.

Contents

Figures

Tables

Chapter 1 Introduction

The field of nonlinear optics is of increasing importance in physics, chemistry and recently even in industry. Many applications require light at parts of the spectrum where lasers are not available. For instance, much recent interest has focused on blue light for communication and data storage. In some cases the light must also be tunable and narrowband, as in the case for spectroscopic applications.

Nonlinear optics arises from the nonlinearity of the induced polarization in materials. Under certain conditions, nonlinear crystals can be used to transfer energy from one wavelength to another. For instance frequency doubling crystals can take infrared light and halve the wavelength to produce blue light. In future this might be used in CD players,[1] rather than developing semiconductor lasers that directly emit blue light.

Optical parametric oscillation is more complex than second-harmonic generation because it involves a resonating cavity around the nonlinear crystal and results in the generation of two beams at different wavelengths. Using a technique called phase matching, the wavelength of these two beams can be varied. In this project, critical phase matching was used, which allows a scan range of hundreds of nanometres to be readily obtained. The theory of nonlinear optics and OPOs is summarized in Chapter 2.

The effects of the nonlinear polarization are generally only observed using strong electric fields, which only became available with the invention of the laser. In 1961, barely a year after Maiman reported the first ruby laser, Franken *et al* observed frequency doubling from a ruby laser in quartz.[2] The effect was not very distinct because their interaction was not phase matched.

The first OPO was demonstrated in 1965 by Giordmaine and Miller[3] who made their cavity by vaporizing mirrors directly onto the ends of a lithium niobate ($LiNbO_3$) crystal. It was pumped by a Nd:$CaWO_4$ laser and their extremely short cavity meant a low threshold energy. Further progress was hindered by the lack of stable, spatially and spectrally pure pump lasers and the poor quality of the low damage threshold crystals. The nonlinear crystal used in this project was β-barium borate, often written β-BaB_2O_4 or β-BBO, and the third harmonic of a *Q*-switched Nd:YAG was used as the pump source. BaB_2O_4 was developed in 1985 by Chen *et al* and features a high damage threshold and a high nonlinear coefficient.[4]

The most significant problem with OPOs at present is that their linewidth is inherently broad.[5] Special linewidth reduction techniques must be used to allow OPOs to reach their full potential as tunable sources of coherent radiation. One method of achieving this reduction is to introduce wavelength-selective elements such as étalons into the cavity. Another is to insert a dispersive element, such as a diffraction grating or a prism, into the cavity.[6][7] In a resonant cavity, only a narrow range of wavelengths will then be resonated effectively, the others will be walked out of the cavity by dispersion.

The limitations of these methods of narrowing the linewidth are the accompanying cavity length extensions and the risk of damage to the intra-cavity elements. Both increased length and intra-cavity elements increase the OPO threshold. An alternative method investigated in this project is injection seeding, where one seeded mode depletes the pump beam before the other modes have time to reach a significant level. The seeded mode is supplied with an initial intensity significantly above the quantum noise level in the crystal. The initial gain experienced by the modes depends on the pump and phase matching conditions and after some time gain saturation sets in.

Seeding was first performed by Bjorkholm and Danielmeyer, who seeded their ruby-laser pumped, two-mirror lithium niobate ($LiNbO_3$) OPO using a cw Nd:YAG laser.[8] Successful seeding requires a suitably intense source of light which also matches the wavelength selected by the OPO crystal and resonant cavity. Seeding has previously been performed in BaB_2O_4 in our laboratory using a fixed wavelength gas laser, where the OPO wavelength was matched to the seed by varying the optical cavity length. Fine control was achieved by changing the temperature of the crystal.[9]

Fix and Wallenstein demonstrated that seeding need not occur at the resonated wavelength. Their seeding was equally successful using a dye laser at the resonant wavelength as a Ti:Sapphire laser at the infrared non-resonant wavelength.[10] This project focuses on the use of a semiconductor laser diode to generate the infrared seed light, since these devices are very cheap and stable and have a narrow bandwidth. They have the added advantage that their output wavelength can be scanned, especially in conjunction with an external cavity.[11][12] This makes it easier to seed the OPO since the seed can easily be matched to the OPO wavelength rather than *vice versa*.

Diode lasers have been used as seed lasers for OPOs, but predominantly when using a three-mirror ring cavity.[13] A ring cavity is often preferred because beams are only travelling in one direction, so there are no back-reflections to the seed laser. Seeding in a ring cavity has also been performed using a Ti:Sapphire laser.[14]

Extensive work was carried out during this project on optimizing a diode laser with optical feedback from a diffraction grating. Once this laser system was operational with a scan range comparable to the best reported literature values it was used for injection seeding at the idler wavelength. The results of the diode scan and the seeding experiments are presented in Chapter 4, after a summary of the equipment used in the project in Chapter 5.

A variable-wavelength seed laser leads to the proposition of scanned seeding, where the OPO wavelength tracks the seed wavelength. Provided the two effects are kept in step, it is possible to maintain OPO seeding. A scanned, seeded OPO would generate high-intensity light with a linewidth comparable to that of the diode, making it a very attractive spectroscopic tool. In a ring cavity, the wavelength of the OPO can be adjusted by moving one of the mirrors,[13] but for this project temperature tuning was envisaged.

A parameter of particular importance when operating an OPO is its threshold, i.e. the input energy at which the oscillation commences. A variety of numerical models is available,[10][14][15] but for the purposes of unseeded operation the simplest and most successful was published by Brosnan and Byer in 1979.[7] The authors found good agreement between their model and experiments performed on a series of $LiNbO_3$ crystals. The second part of this project investigated the effects of varying pump spotsize, OPO cavity length and output coupler on the oscillator threshold fluence. The values were compared to the simplified model of Brosnan and Byer, where a square pump pulse temporal profile is assumed.

Chapter 2 Theory

2.1 Lorentz Model

The classical Lorentz model of the atom treats the electron as being tied to the nucleus by a spring. In the absence of an electric field, the positive charges from the nuclei and the negative charges from the electrons are distributed to produce a non-polarized solid. When an electric field **E** is applied to the solid, the electron experiences a Lorentz force **F** given by

$$\mathbf{F} = -e\mathbf{E}, \quad (1)$$

where e is the charge of the electron, and this force moves the electron from its equilibrium position by an displacement **r**. Although the nucleus is also charged, it is assumed that only the electron moves because the nuclear mass is significantly greater than the mass of the electron. The displacement upsets the balanced charge distribution and introduces a polarization **P** into the medium, given by

$$\mathbf{P} = -Ne\mathbf{r} \quad (2)$$

where N is the number density of valence electrons in the solid. The model assumes that the spring between the electron and the nucleus obeys Hooke's law, so that when the electrostatic force from the field is balanced by the restoring force of the spring, the displacement **r** is directly proportional to **E**. Hence the polarization is also proportional to the electric field, and the constant relating the two is called the susceptibility and denoted χ. In S.I. units χ is scaled by ε_0, the permittivity of free space, to become a dimensionless quantity and we write

$$\mathbf{P} = \varepsilon_0 \chi \mathbf{E}. \quad (3)$$

If we apply an oscillating electric field in the form

$$\mathbf{E} = \mathbf{E}_0 \cos \omega t \quad (4)$$

to the medium, the model predicts that the electron is accelerated back and forth, so that it emits an electric field at the same frequency, but with a phase lag due to the inertia of the electron. The resultant electric field is the sum of the incident and the re-radiated fields, at the same frequency ω but with a net phase lag.

The Lorentz model accounts for the refractive index

$$n = \frac{c}{v_{\text{medium}}} \quad (5)$$

by assuming that when the electric field travels along a line of electrons, they form a phased array of antennae such that the resultant field is cancelled by destructive interference in all

but the forward direction. The overall phase lag when the electric field wave emerges from the solid accounts for the observation that it travels more slowly in the medium than outside.

2.2 Nonlinearity

The linear model described above fails in certain situations when effects that are usually obscured become significant. In the present discussion, this leads to the field of nonlinear optics.

2.2.1 Nonlinear Polarization

The assumption that the displacement of the electron from equilibrium is directly proportional to the applied electric field is only valid if the field strength is weak. If the applied electric field strength becomes comparable to the interatomic fields, then the relationship between the polarization and the electric field is no longer linear. We can extend equation (3) as a Taylor series and write[16]

$$P = \varepsilon_0(\chi^{(1)}E + \chi^{(2)}E^2 + \chi^{(3)}E^3 + \ldots). \quad (6)$$

In this equation, the notation for the linear susceptibility in equation (3) is changed from χ to $\chi^{(1)}$ in order to accommodate $\chi^{(2)}$ and $\chi^{(3)}$, the second and third-order nonlinear susceptibilities. It should be noted that $\chi^{(2)}$ and $\chi^{(3)}$ are not dimensionless like $\chi^{(1)}$, so calling them susceptibilities can be somewhat misleading. Contributions from increasing order terms become increasingly insignificant and terms higher than second order are almost always negligible. In third-order nonlinear materials, the second-order effects are often suppressed because a crystal symmetry condition requires $\chi^{(2)} = 0$. This dissertation will neglect third order terms and higher because they are insignificant in BaB_2O_4. Hence the polarization is written as

$$P = \varepsilon_0(\chi^{(1)}E + \chi^{(2)}E^2). \quad (7)$$

If an electric field with two distinct frequencies ω_1 and ω_2 and amplitudes E_1 and E_2 is applied to a second-order nonlinear material, equation (7) yields a polarization containing the terms

$$\begin{aligned} P_{\text{DC}} &= \varepsilon_0\chi^{(2)}(E_1^2 + E_2^2) \\ P_{\text{harmonic}} &= \varepsilon_0\chi^{(2)}(E_1^2\cos 2\omega_1 t + E_2^2\cos 2\omega_2 t) \\ P_{\text{sum}} &= \varepsilon_0\chi^{(2)}(E_1E_2\cos(\omega_1 + \omega_2)t) \\ P_{\text{difference}} &= \varepsilon_0\chi^{(2)}(E_1E_2\cos(\omega_1 - \omega_2)t) \end{aligned} \quad (8)$$

as well as the fundamental frequency components from the linear polarization term. The DC polarization is the basis for the electro-optic effect, where an electric field is used to control the optical properties of a material, while the polarizations at $2\omega_1$ and $(\omega_1 + \omega_2)$ are used in second-harmonic and sum-frequency generation respectively. For instance, in the Nd:YAG pump laser used for this project, one KD*P crystal frequency-doubles the infrared generated by the laser rods to green light. Another then combines this with the original light to produce ultraviolet at three times the fundamental frequency.

2.2.2 Three-wave Interaction

The sum and difference frequencies in equation (8) are of particular interest when discussing OPOs. We consider the situation described, with fields at ω_1 and ω_2 incident on the material, and define a sum frequency

$$\omega_3 = \omega_1 + \omega_2. \quad (9)$$

Through P_{sum}, waves ω_1 and ω_2 give rise to ω_3 in the material, but since now $\omega_1 = \omega_3 - \omega_2$, ω_3 and ω_2 can interact and produce ω_1 from the $P_{\text{difference}}$ term. Similarly, ω_3 and ω_1 can generate ω_2. This cyclic process is called the three-wave interaction. The waves with frequencies ω_1, ω_2 and ω_3 are called the signal, the idler and the pump respectively. For the experiments discussed in this dissertation, the convention adopted is that the pump is the fixed wavelength ultraviolet Nd:YAG beam and the signal and idler beams are generated by the OPO. The signal and idler wavelengths can be varied and there is no inherent difference between the two except that one is resonated in the cavity. The signal is the resonated, lower wavelength visible light, while the idler is in the infrared. Although an infinite number of wavelength pairs (ω_1, ω_2) can satisfy equation (9), in practice further criteria must be satisfied before an effective three-wave mixing process can occur.

2.2.3 Parametric Amplification

If only the pump and signal beams, i.e. ω_3 and ω_1, are incident on a nonlinear crystal, then the amplitude of the difference frequency polarization of equation (8) is proportional to E_1E_3. Hence a significant amount of ω_2 can be generated even if the signal intensity is weak, provided that the pump has a high amplitude. The pump and ω_2 can then interact to generate more of the signal, the net result being that the amplitude of ω_1 grows. This is termed optical parametric amplification.

Optical parametric oscillation is a modification of this, where only the pump is applied to the material. The signal and idler beams are generated from the quantum noise inside the medium and amplified by resonation in a cavity. The nonlinear material and the resonating cavity together are called an optical parametric oscillator or OPO. Equation (9) can be regarded as a photon conservation equation: For each signal photon generated, an idler photon is generated as well. Thus resonating either only the signal or only the idler is sufficient to amplify both beams. A situation where only one is resonated is termed singly resonant operation (SRO) to distinguish it from double resonance, denoted DRO. The OPO used in this project was singly resonant.

An OPO exhibits shot-to-shot jitter, where the output is not constant between successive pulses, because the signal and idler beams build up in each case from random noise. Injection seeding provides an initial intensity at the seed wavelength which may be equal to either the signal or the idler wavelength.[10] Provided that the seeded mode is near the centre of the gain profile of the OPO, it will be amplified and deplete the pump before other modes build to significant levels, thus reducing the linewidth of the device. Seeding also reduces the build-up time.

Since the pump beam has a significantly higher intensity than the signal and idler beams, the predominant flow of energy is from the pump to the signal and idler wavelengths, but back-conversion can occur if the signal and idler beams become sufficiently intense. In this case it is possible for the depleted pump temporal profile to have a series of oscillations due to the repeated depletion and back-conversion processes.

2.2.4 Coupled Rate Equations

For a more detailed analysis of the three-wave interaction in an OPO, the nonlinear polarization from equation (7) must be included as a source term in Maxwell's equations. In one dimension, this leads to[18]

$$\frac{d^2E}{dz^2} = \mu_0\varepsilon\frac{d^2E}{dt^2} + \mu_0\frac{d^2P}{dt^2}. \quad (10)$$

For simplicity, the interaction is restricted to three plane wave fields at frequencies ω_i described by

$$E(\omega_i) = E_i e^{-i(k_i z - \omega_i t)},\ i = 1, 2, 3. \quad (11)$$

Here the E_i are the complex amplitudes and $k_i = 2\pi/\lambda_i$ are the wavenumbers of the signal, idler and pump fields. The solution of equation (10) leads to the coupled differential equations[7][18]

$$\begin{aligned}
\frac{dE_1(z)}{dz} + \alpha_1 E_1 &= -i\omega_1\sqrt{\frac{\mu_0}{\varepsilon_1}}\varepsilon_0\chi^{(2)}E_2^*(z)E_3(z)e^{-i\Delta kz} \\
\frac{dE_2(z)}{dz} + \alpha_2 E_2 &= -i\omega_2\sqrt{\frac{\mu_0}{\varepsilon_2}}\varepsilon_0\chi^{(2)}E_1^*(z)E_3(z)e^{-i\Delta kz} \quad (12) \\
\frac{dE_3(z)}{dz} + \alpha_3 E_3 &= -i\omega_3\sqrt{\frac{\mu_0}{\varepsilon_3}}\varepsilon_0\chi^{(2)}E_1(z)E_2(z)e^{+i\Delta kz}
\end{aligned}$$

which relate the amplitudes of the three fields in the medium. In equations (12), the ε_i are the relative permittivities of the medium at frequencies ω_i and the α_i the corresponding absorption coefficients. Further,

$$\Delta k = k_3 - k_1 - k_2 \quad (13)$$

is the mismatch between the pump, signal and idler *k*-vectors. The physical interpretation of Δk is that the interacting waves become out of phase with each other, which means that effective coupling cannot be achieved unless $\Delta k \approx 0$.

Equations (12) can be solved analytically, but for most purposes a simplified expression is adequate. The effects of anisotropy are introduced before an expression for the signal single pass gain is derived in section 2.6.

2.3 Anisotropy

The refractive index of a medium is influenced by the interaction between the atoms in the medium, and it is possible for the refractive index to depend on the direction of the applied electric field. Materials which exhibit this phenomenon are called anisotropic.

Mathematically, the susceptibilities in Equation (7) become tensors, and adopting the Einstein convention of summing over repeated indices we write

$$P_i = \varepsilon_0(\chi_{ij}^{(1)}E_j + \chi_{ijk}^{(2)}E_jE_k). \quad (14)$$

From equation (14) it is clear that $\chi_{ijk}^{(2)}$ is symmetric in *j* and *k*, so we can define a single index *l* to replace the permutations of *j*, *k* and write $\chi_{il}^{(2)}$, where *l* runs over $l = 1, 2, \ldots, 6$. This reduces the number of independent components of $\chi_{ijk}^{(2)}$ from 27 to 18, although in practice many of the $\chi_{il}^{(2)}$ are zero.

2.3.1 Uniaxial Crystals

In a uniaxial crystal, one of the crystallographic axes has a different refractive index to the other two. This axis is labelled the optic axis and is defined as lying in the *z*-direction. The refractive index for a polarization along the optic axis is called the extraordinary refractive index, n_e, to distinguish it from the refractive indices for polarizations along the other axes, which are called ordinary and denoted n_o.

Any polarization vector can be resolved into components parallel and perpendicular to the optic axis, so a general polarization will see a refractive index between n_o and n_e. A beam whose polarization is perpendicular to the optic axis, i.e. a beam which sees n_o, is termed an ordinary beam, while extraordinary beams have polarization components along the optic axis.

Uniaxial crystals can be separated into two further categories, depending on the relative magnitudes of n_o and n_e. If $n_e - n_o > 0$, the material is called positive, and if $n_e - n_o < 0$ it belongs to the negative class. BaB_2O_4 is a negative uniaxial crystal.

In a biaxial crystal there are three different characteristic refractive indices and two mutually orthogonal optic axes. These are outside the scope of this dissertation.

2.3.2 Index Ellipsoid

The dependence of *n* on the direction of polarization can be displayed using the index ellipsoid,[19] also known as the optical indicatrix, as in Figure 2-1.

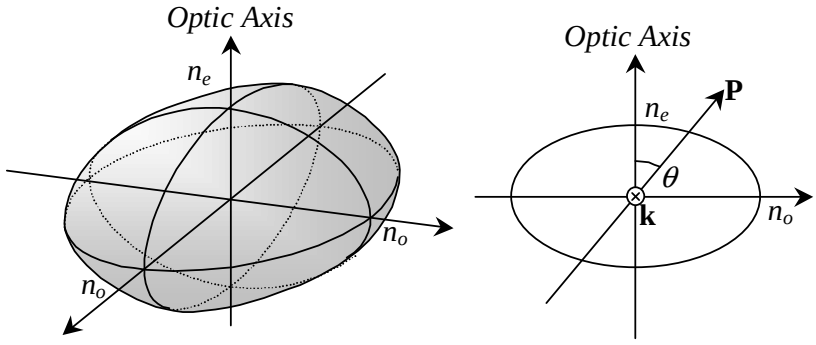

Figure 2-1: Index Ellipsoid and Projection

If we consider a beam with a given **k**-direction, then its polarization **P** must lie in the plane perpendicular to **k**. The intersection between this plane and the index ellipsoid is an ellipse and gives the dependence of *n* on the direction of polarization. For a given polarization, the distance between this ellipse and the origin, parallel to the polarization, is the refractive index that the wave sees.

For an extraordinary beam, the refractive index dependence on angle can be calculated using simple geometric arguments and is found to be

$$n(\theta) = \frac{n_o n_e}{\sqrt{n_e^2 \cos^2\theta + n_o^2 \sin^2\theta}} \quad (15)$$

where θ is the angle between the polarization and the optic axis inside the crystal.

2.3.3 Poynting Vector Walkoff

The Poynting vector of an electromagnetic field, defined as

$$\mathbf{S} = \frac{1}{\mu_0}\mathbf{E} \times \mathbf{B}, \quad (16)$$

represents the direction of energy flow and is perpendicular to the refractive index curve.[19] Thus an extraordinary beam experiences Poynting vector walk-off, where **S** is not perpendicular to the electric field wave fronts. Figure 2-2 shows the walk-off angle ρ, which is defined as the angle between **S** and **k**.

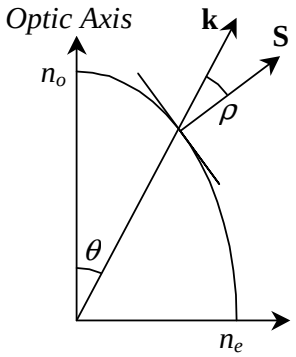

Figure 2-2: Poynting Vector Walk-Off

Poynting vector walk-off places an upper limit on the useful crystal length, called the walk-off length and denoted l_w. The parametric interaction cannot be supported for distances greater than l_w because the energy is no longer coupled from the pump into the signal and idler beams. If the electric field radii of the pump and signal beams are denoted w_3 and w_1 respectively, then the walk-off length is[7]

$$l_w = \frac{\sqrt{\pi}}{2}\frac{w_3}{\rho}\sqrt{\frac{{w_3}^2 + {w_1}^2}{{w_3}^2 + {w_1}^2/2}}\,. \quad (17)$$

2.4 Phase Matching

In order to generate a significant amount of coherent light at the signal and idler wavelengths, the three interacting waves must remain in constant phase relationship throughout the crystal. Due to normal dispersion, waves with different wavelengths travel at different

velocities through the medium, so this criterion will in general not be satisfied. For the parametric interaction to occur over an extended region in the crystal, dispersion must be compensated, which is equivalent to setting the phase mismatch Δk in equation (13) to zero.

Generally the refractive index for a material is a function of the polarization and wavelength of the light and the temperature of the crystal. The equations defining $n(\mathbf{P}, \lambda, T)$ are called the Sellmeier equations. It is possible to achieve phase matching by varying parameters other than the wavelength. In critical phase matching, the polarization and propagation angles to the optic axis are varied, which leads to angle tuning, as discussed below. Non-critical phase matching involves changes in temperature to compensate for the wavelength dependence of n.

2.4.1 Critical Phase Matching

In our OPO phase matching was achieved by making use of the anisotropy of BaB_2O_4. The pump was chosen to be an extraordinary beam and its angle relative to the optic axis selected such that a particular signal and idler pair are phase matched. The pump, signal and idler wavelengths then satisfy

$$\begin{aligned} \frac{1}{\lambda_3} &= \frac{1}{\lambda_1} + \frac{1}{\lambda_2} \\ \frac{n(\theta)}{\lambda_3} &= \frac{n_o}{\lambda_1} + \frac{n_o}{\lambda_2} \end{aligned} \quad (18)$$

where $n(\theta)$ is the refractive index that the pump beam sees. This type of phase matching is called Type I. Another way of achieving critical phase matching in an anisotropic crystal is called Type II, where either the signal or the idler beam as well as the pump is extraordinary.

2.4.2 Collinearity

In the general case, equation (13) is a vector relationship, which means that the pump, signal and idler **k**-vectors can satisfy $\mathbf{\Delta k} = \mathbf{0}$ without necessarily being parallel. The two situations shown in Figure 2-3 are called collinear and non-collinear respectively.[20] Throughout the course of the experiments presented, collinear phase matching was used.

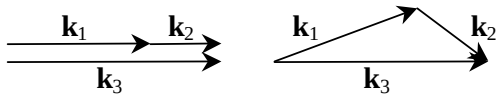

Collinear *Non-Collinear*

Figure 2-3: Collinear and Non-Collinear Phase Matching

2.5 Nonlinear Coefficient

In practice, the nonlinear coefficient d is used rather than $\chi^{(2)}$ in equation (7), where $\chi^{(2)} = 2d$. Thus d is also a third-rank tensor contracted in the same way as $\chi^{(2)}$, so the nonlinear polarization can be written in matrix form as

$$\begin{bmatrix} P_x^{(2)} \\ P_y^{(2)} \\ P_z^{(2)} \end{bmatrix} = 2\varepsilon_0 \begin{bmatrix} d_{11} & d_{12} & d_{13} & d_{14} & d_{15} & d_{16} \\ d_{21} & d_{22} & d_{23} & d_{24} & d_{25} & d_{26} \\ d_{31} & d_{32} & d_{33} & d_{34} & d_{35} & d_{36} \end{bmatrix} \begin{bmatrix} E_x^2 \\ E_y^2 \\ E_z^2 \\ 2E_yE_z \\ 2E_xE_z \\ 2E_xE_y \end{bmatrix}, \quad (19)$$

although for real materials most d_{il} are zero. Nonetheless, equation (19) is cumbersome to use, so an effective nonlinear coefficient d_{eff} is calculated for each specific interaction. A particular interaction refers to a defined orientation of the three interacting beams. For a type I interaction in β-BaB_2O_4,[4]

$$d_{eff} = d_{31}\sin\theta - d_{22}\cos\theta\sin 3\phi. \quad (20)$$

Here θ is the polar and ϕ the azimuthal angle of the extraordinary beam polarization to the optic axis inside the medium. The effective nonlinear coefficient simplifies equation (19) to

$$P^{(2)} = 2\varepsilon_0 d_{eff} E^2. \quad (21)$$

2.6 Single Pass Gain

By making suitable approximations, equations (12) can be solved for the small signal single pass gain experienced by the signal beam. It is assumed that the pump beam depletion is negligible, i.e. $dE_3/dz = 0$, that the absorption coefficients for the signal and idler are equal at $\alpha_1 = \alpha_2 = \alpha$ and that the idler field is zero at the entrance of the crystal. The signal field at the end of a crystal of length l is then[7]

$$E_1(l) = E_1(0)\, e^{-\alpha l} \cosh \Gamma L \quad (22)$$

where

$$\Gamma = \frac{\chi^{(2)}}{c}\sqrt{\frac{\omega_1\omega_2}{\varepsilon_1\varepsilon_2} g_s |E_3|^2} \quad (23)$$

is the parametric gain coefficient and

$$L = l_w \operatorname{erf}\left(\frac{\sqrt{\pi}}{2}\frac{l}{l_w}\right) \quad (24)$$

an effective gain length. Here l_w is the walk-off length given in equation (17). The error function approaches unity for large arguments, so the walk-off length is the effective gain length for an infinitely long crystal. In equation (23),

$$g_s = \frac{w_3^2}{w_3^2 + w_1^2} \quad (25)$$

is the signal spatial mode coupling coefficient, where the w_i are the field radii.

From equation (22) the single-pass power gain becomes

$$\frac{|E_1(l)|^2}{|E_1(0)|^2} = e^{-2\alpha l} \cosh^2 \Gamma L, \quad (26)$$

where Γ has a local maximum at $\omega_1 = \omega_2$, called degeneracy. Oscillation threshold is reached when the single pass gain from equation (26) exactly balances the round-trip losses. Measurements of the influence of OPO parameters on threshold are discussed in Chapter 5.

Chapter 3 Equipment

This chapter records the devices used for observing and collecting the data presented in this dissertation. Since a substantial part of the project involved work on the diode laser, it is included separately in section 4.1 below.

3.1 Optical Parametric Oscillator

The OPO comprised the nonlinear crystal and a plane-plane resonant cavity shown in Figure 3-1. Some of the mechanical supports have been omitted for clarity. This device was first investigated in 1996 by Noah Russell who went on to study the effects of collinearity and successfully performed injection seeding at a signal wavelength of 633 nm to narrow the linewidth.[9]

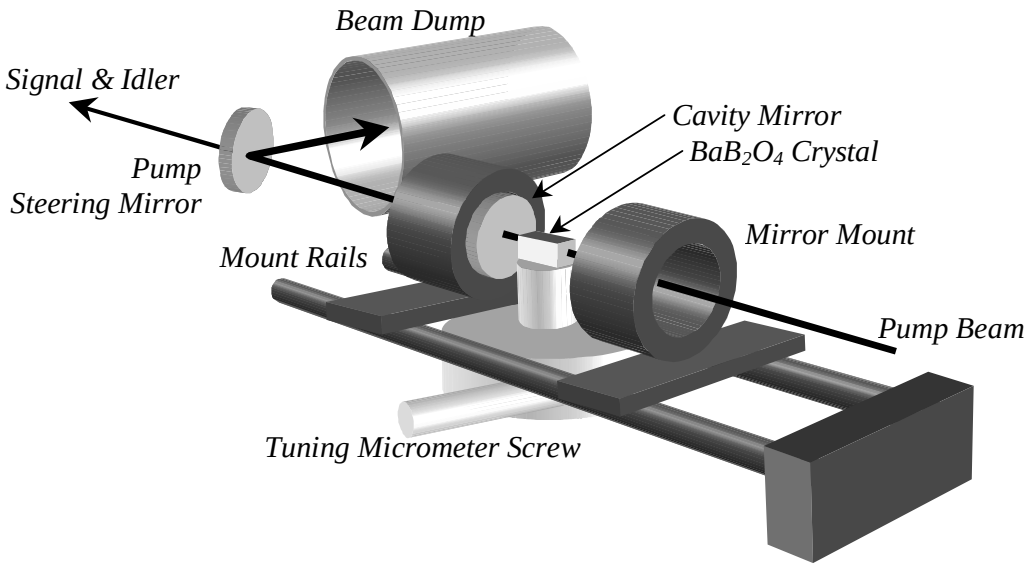

Figure 3-1: OPO Cavity

3.1.1 BaB_2O_4 Crystal

The nonlinear crystal used in this project was barium borate (β-BaB_2O_4 or BBO) with dimensions 6 × 6 × 12 mm. The front and rear faces were polished but uncoated since anti-reflection coatings have a lower damage threshold than BaB_2O_4 itself. The crystal was cut at $\theta = 33°$ and $\phi = 90°$ with respect to the optic axis in order to maximise the nonlinear coefficient. Table 3-1 summarizes crystal data obtained from the Handbook of nonlinear optical crystals.[4] Standard symbols are used throughout the dissertation.

Parameter	*Symbol*	*Value*
Nonlinear Coefficient	d_{eff}	2.02 pm/V
Damage Threshold	J_{thr}	152 Jcm^{-2}
Absorption Coefficient	α	0.01 cm^{-1}
Walk-off Angle	ρ	4.132°
Refractive Index Temperature Dependence	$\frac{dn_o}{dT}$	-16.6×10^{-6} K^{-1}
	$\frac{dn_e}{dT}$	-9.3×10^{-6} K^{-1}

Table 3-1: BaB_2O_4 Parameters

The effective nonlinear coefficient d_{eff} can be calculated from the tabulated values of d_{22} = 2.3 pm/V and d_{31} = 0.16 pm/V and equation (20). In the threshold modelling below, a range values for d_{eff} of 1.7 to 2.6 pm/V reported by [18] was used.

The damage threshold is of particular importance for obvious reasons. The parameter given in [4] is the damage intensity, I_{thr} = 19 $GWcm^{-2}$ for 1800 pulses at 355 nm, with each pulse being 8 ns long, although recorded values differ between sources. For a Gaussian intensity profile beam with a diameter of 2 mm this corresponds to an energy of around 2 J per pulse. Since optical coatings often have damage thresholds lower than this, pump energies used did not exceed 15 mJ per pulse for beam diameters below 5 mm. The damage threshold scales as the square root of the pulse width.[21]

The linear absorption coefficient α and walk-off angle ρ are explained in sections 2.2.4 and 2.3.3 respectively, are used in the threshold investigation in Chapter 5 below. Both are quoted for a signal wavelength of 532 nm.

The temperature dependence of the refractive index is important for predicting the behaviour of the OPO modes as the temperature is changed, as described in section 4.4.3. Since the resonated signal is an ordinary beam, only dn_o/dT is of interest.

The Sellmeier equations for BaB_2O_4 at 20 °C can be expressed as[4]

$$n_o^2 = 2.7359 + \frac{0.01878}{\lambda^2 - 0.01822} - 0.01354\lambda^2$$
$$n_e^2 = 2.3753 + \frac{0.01224}{\lambda^2 - 0.01667} - 0.01516\lambda^2, \qquad (27)$$

where the λ are in μm. Since dn/dT is small, the effect of the difference between quoted and operating temperatures is negligible. The first of equations (27) is plotted in Figure 3-2 for a

range of signal and idler wavelengths. Both equations are used in the threshold study in Chapter 5.

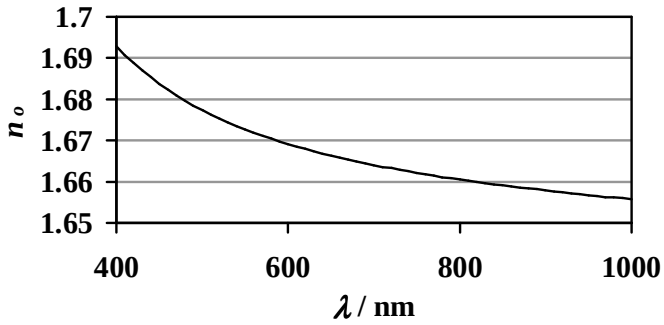

Figure 3-2: Ordinary Refractive Index with Wavelength

The BaB_2O_4 crystal was enclosed in a mount to preclude accidental damage to the crystal faces. To prevent water absorption, which could degrade the optical quality of the crystal and potentially cause laser damage, the crystal was held at approximately 40 °C. When not in use it was also kept in an atmosphere of nitrogen. The micrometer screw shown in Figure 3-1 allowed the crystal mount to be accurately turned through small angles independently of the rest of the cavity. Since these changes caused the OPO to be phase matched for different frequencies, it is termed the tuning micrometer screw.

3.1.2 Temperature Control

Since the temperature of the crystal determined the optical cavity length and was used to scan the cavity modes, it was important that the temperature be stabilized. To this end, a thermistor and a heater were embedded into the crystal mount and controlled by a feedback system to maintain a constant temperature.

The thermistor was supplied with a constant current of $I = 101.4\ \mu A$ so that its temperature-dependent resistance could be converted into a voltage according to $V = IR$ which was displayed on a 6-digit digital voltmeter. The response had been previously calibrated and the temperature T for a given resistance R was found to obey

$$\frac{1}{T} = 1.13198\times10^{-3} + 2.33459\times10^{-4}\ \ln R + 9.10832\times10^{-8}\ (\ln R)^3. \quad (28)$$

The curve temperature of T as a function of measured voltage V is shown in Figure 3-3.

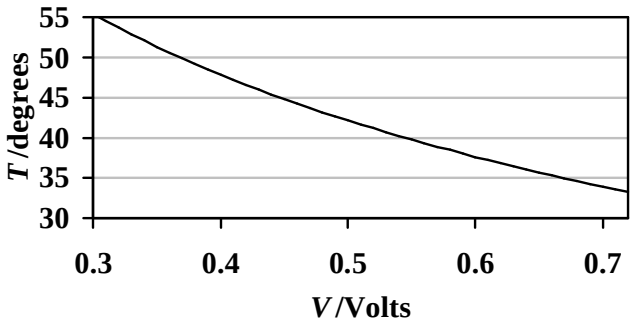

Figure 3-3: OPO Temperature Curve

3.1.3 Resonant Cavity

The resonant cavity was formed by plane mirrors in stable Melles Griot Flexure mirror mounts, which could be moved on the rails shown in Figure 3-1 to lengthen or shorten the cavity. For normal operation, the cavity length was chosen to be as short as possible, so that the resonated signal had the maximum number of round-trips during the pump pulse and thus the highest overall gain.

Figure 3-1 also shows the positioning of the beam dump. Since it was possible for the pump beam to pass through the cavity without experiencing depletion, for instance if the crystal were misaligned, it had to be discarded before the OPO output was subjected to any diagnostic tests. For convenience, the beam dump was kept as close as possible to the output coupler of the cavity. The mirror used to reflect the pump into the beam dump was identical to the other pump steering mirrors, since had the required high damage threshold and were virtually transparent at the signal and idler wavelengths.

3.1.4 Tuning Curve

One of the most attractive features of an OPO is its extremely broad tuning range, as indicated in Figure 3-4.[9] For any angle of the pump beam to the optic axis, intersections of the appropriate line with the tuning curve give the idler and signal wavelengths. The two curves would meet at exactly half the pump wavelength at a point called degeneracy, but the cavity mirror reflectivities did not support oscillation beyond about 700 nm.

The following page contains two photographs of the OPO operating at different wavelengths. The view is similar to that in Figure 3-1.

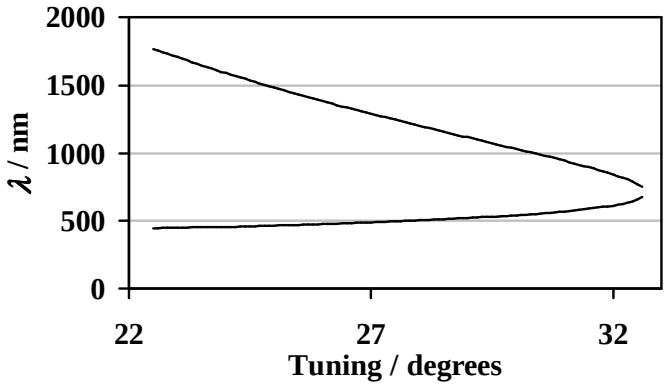

Figure 3-4: OPO Tuning Curve

3.2 Pump Laser

The laser used to pump the OPO was an Nd:YAG Continuum Powerlite PL7000, frequency-tripled to produce ultraviolet light at 354.73 nm. The laser was operated at 10 pulses per second. The energy per pulse could be adjusted by changing the *Q*-switch delay after the onset of the flash lamp discharge. As explained in section 3.1, pump energies were kept substantially below the published damage thresholds of BaB_2O_4.

The Nd:YAG oscillator was injection-seeded using a diode-pumped Nd:YAG MISER system inside the Powerlite case to stabilize the frequency of the output. This also had the effect of reducing the pulse width, because the pulse did not need to build up from spontaneous emission. The cavity length of the Nd:YAG laser was adjusted during each pulse to correct for drifts in the YAG rods, but if the energy dropped below about 2 mJ per pulse then the locking mechanism failed and the pulse width increased dramatically.

A brief investigation into the dependence of pulse duration on pulse energy was conducted. The results are shown in Figure 3-5. The pulse duration τ was taken to be the full width at half maximum (FWHM) of the temporal profile, where the pulses are approximately Gaussian in shape.

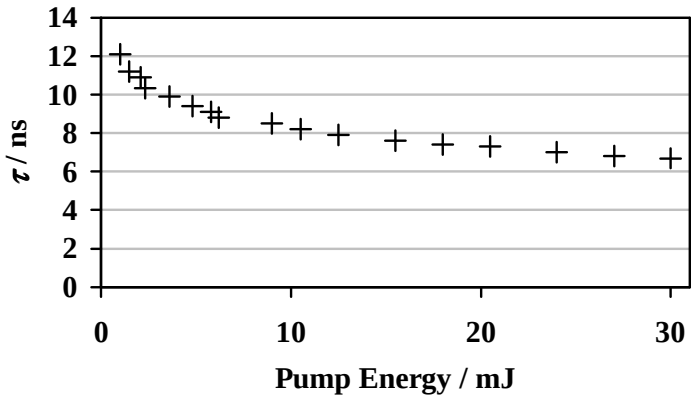

Figure 3-5: Pump Pulse Duration

Since the variation of pulse length over the 5-15 mJ per pulse energy range used is minimal, a fixed FWHM pulse duration of 8 ns was assumed for the threshold modelling.

3.3 Table Layout

Figure 3-6 shows the physical layout of the components on the Newport RP Reliance anti-vibration optical table top. The table top was supported on Newport Series I-2000 Laminar Flow Isolators. It was important to eliminate as many of the acoustic vibrations as possible, since they severely affected the stability of the diode laser and OPO cavities.

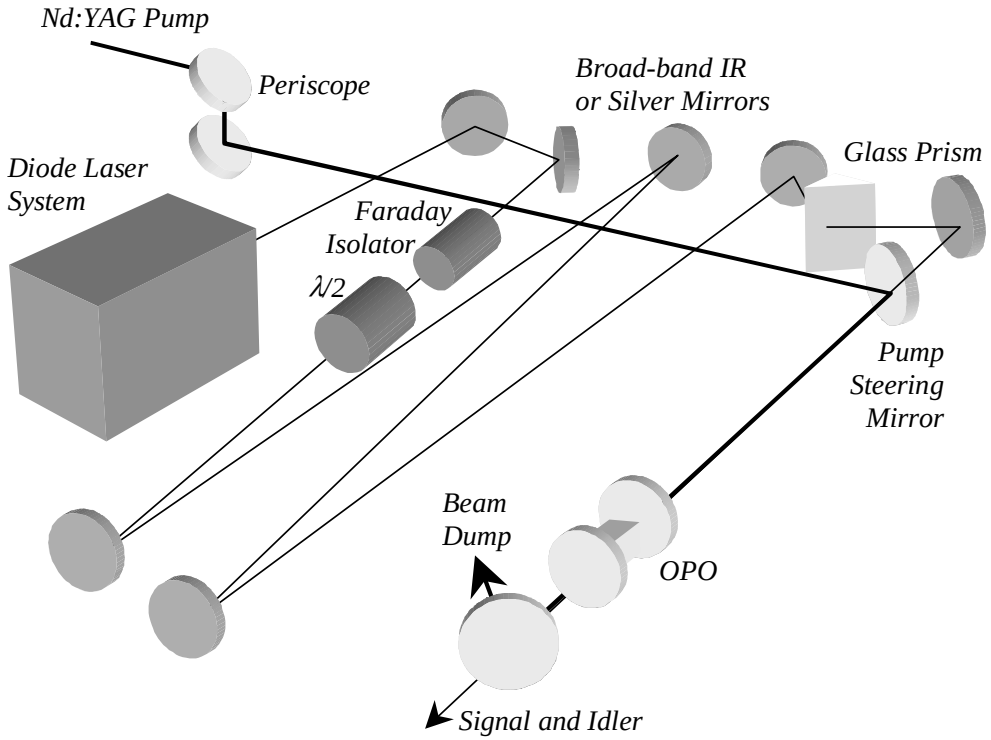

Figure 3-6: Optical Table Layout

There were two separate beam paths superimposed due to space restrictions. The Nd:YAG pump beam was taken from the laser output port to the standard height of 121 mm above the table surface by a periscope. A single pump steering mirror passed the beam through the BaB_2O_4 crystal, after which the depleted beam was deposited in the beam dump. The second more complex beam path involved the seed beam. The long path length and the additional optics protected the seed laser from back-reflections from the OPO and are described in detail in section 4.2 below.

3.4 Power Meter

A Laser Instrumentation Model 6000 thermal power meter was used to measure beam powers. Thermal power meters have a very wide operating range, both in terms of wavelength and energy, and their response does not need to be re-calibrated when the wavelength changes. Their main disadvantage is that their response is slow, so it was not possible to measure the energy of a single pulse directly. The power meter displayed a time averaged power which could be easily converted into an energy per pulse by dividing by the repetition rate.

3.5 Infrared Detection

The human eye fails to detect light above about 800 nm, so in order to see the seed and idler beams, IR cards or viewers were used. This was necessary for finding the beam when aligning the silica fibre and étalons or at the output of the spectrometer. IR detector cards absorb energy at ultraviolet wavelengths, for instance from fluorescent tubes, and fluoresce red when IR light falls on them. They are ideal for finding a beam of significant intensity, but they have a restricted response bandwidth. IR viewers are hand-held devices which amplify an infrared image by accelerating electrons ejected by the photoelectric effect onto a phosphor screen. They offer more detail and a better response than IR cards.

3.6 Photodiodes

Photodiodes were used for detecting weak and rapidly changing signals. They are very similar to semiconductor lasers and LEDs, except that the predominant process is excitation of electrons by photons. Throughout the project, FND100 p-i-n silicon photodiodes were used. They were operated with a 90-V reverse bias and had a linear response curve provided the output current did not exceed 20 mA.

3.7 Display Devices

Signals from the photodiodes and the various driving electronics were displayed using two different oscilloscope models. To take large-scale lineshape profiles of the OPO signal and idler beams, only possible by slowly scanning the spectrometer, the pulsed photodiode signal was first passed through a boxcar integrator which integrated the signal across a variable gate and held the value until the next pulse arrived. For most applications, a Tektronix TDS 350 oscilloscope with a maximum sampling rate of 1 GS/s was used. Data was transferred to a computer using an IEEE standard GPIB cable and the accompanying program called WaveStar. In some instances, an Hewlett-Packard HP 54522A oscilloscope was used instead of the Tektronix model. The HP scope had a built-in PC format disk drive and either a 1 MΩ or 50 Ω input impedance. Its highest sampling rate was 2 GS/s.

3.8 Spectral Analysis

One of the most important parameters of an OPO is its output spectrum. Spectral measurements carried out included coarse analysis to tune the crystal so that the free-running idler wavelength matched the seed as well as high frequency-resolution analysis to determine whether seeding was successful or not.

3.8.1 Spectrometer

Coarse spectral measurements were made using a Spex 1500SP spectrometer, the resolution of which depended on the size of the illuminated diffraction grating and the entry and exit slits. For all measurements given in this dissertation, both slits were set to 20 μm or less, which corresponds to an resolution of better than ±0.5 nm. This resolution was sufficient for determining the operating wavelengths and coarse lineshape profiles.

3.8.2 Fibre Patchcord

To obtain results from the spectrometer, the input beam was aimed very accurately along the axis of the input slit. The time-consuming alignment process was avoided by the use of a silica fibre, which took beams coupled into it anywhere in the laboratory and delivered them to the spectrometer reproducibly along the correct path.

Due to its specified damage threshold of 5 GW/cm^2 and diameter of 200 μm, pulses over 10 mJ could not be passed through the fibre. The only beams delivered through the fibre in this project were the < 30 mW cw seed beam and the OPO output when reflected off a glass

plate. The total energy at signal and idler wavelengths after the ≈ 4% reflection did not exceed 100 μJ per pulse.

3.8.3 Fabry-Pérot Interferometer

Three different solid fused silica Fabry-Pérot étalons were used during the experiment to obtain high detail spectral information. The relevant parameters are given in Table 3-2.

Thickness (d)	*Free Spectral Range (FSR)*	*Finesse*
20 mm	5 GHz	35
7 mm	14 GHz	25
1 mm	100 GHz	23

Table 3-2: Fabry-Pérot Etalons Used

The free spectral range is the maximum frequency difference observable before the fringe pattern repeats and is calculated using the standard equation for mode separation,

$$\text{FSR} = \frac{c}{2nd}, \quad (29)$$

where n is the refractive index of the étalon. The finesse gives the ratio of the minimum measurable frequency change to the FSR and is measured by observing the fringes of a very narrow linewidth source.

The étalons were placed after a cylindrical lens which spread the incident beam in the horizontal plane and generated a slice through the standard ring pattern produced by Fabry-Pérot interferometers. The interference pattern was focused onto a CCD camera by an achromatic lens. Once the fringes had been loaded in numerical format on a computer, they were linearized by scaling the x-axis according to $x \rightarrow x^2$.

3.8.4 CCD Camera

An Ikegami black-and-white CCD model ICD-42E camera was used for measuring spatially-distributed intensity patterns such as beam cross-sections, and in conjunction with the Fabry-Pérot étalon to measure high resolution linewidths. The CCD had a resolution of 512 × 582 pixels, vertically interlaced, with the images being returned in 256 intensity levels. The physical size of the CCD array was 6.53 × 4.89 mm.

The images generated by the CCD camera were recorded onto computer using a frame-grabber card and the accompanying program named Pipint, which allowed the use of false-colour shading to enhance subtle intensity differences. The images were analysed on Matlab using some simple programs written by the author.

Chapter 4 Injection Seeding

4.1 Diode Laser

The source of the seed beam used for injection seeding in the OPO was a semiconductor laser diode with optical feedback from an external cavity. The external cavity was constructed by the Mechanics Workshop but much of this project was spent on improving the diode laser performance.

4.1.1 Laser Diode

Laser diodes, which are used for many applications in industry, spectroscopy and atomic physics, are commercially available for operation in a large range of wavelengths and emission powers. Most readily available are diodes near 780 nm or 850 nm, but the precise wavelength of each diode varies by several nm from device to device. The operating region around 850 nm was chosen in order to move as far away from degeneracy of the OPO as possible, thus ensuring single resonance of the cavity. An idler wavelength λ_2 = 850 nm corresponds to a signal wavelength λ_1 = 610 nm.

Semiconductor diodes have extremely wide gain profiles, of the order of tens of nm, but usually operate in single longitudinal mode which corresponds to a linewidth of a few tens of MHz. The semiconductor stripe generating the light is a few tenths of a mm thick and its refractive index is roughly n = 3.5, so adjacent longitudinal modes are separated by several hundred GHz. The diode emission wavelength can be tuned by variation of the injection current or the diode temperature, but it can be tuned continuously only over certain regions before mode 'hopping' occurs. When this happens, the present operating mode is supplanted by one which experiences higher gain for the given conditions. Mode hopping results in a change in emission wavelength and intensity. An example of the dependence of the free-running diode wavelength on injection current and diode temperature is given in Figure 4-1. Increasing temperature settings correspond to higher temperatures. The mode hops are clearly visible as step discontinuities in the emission wavelength.

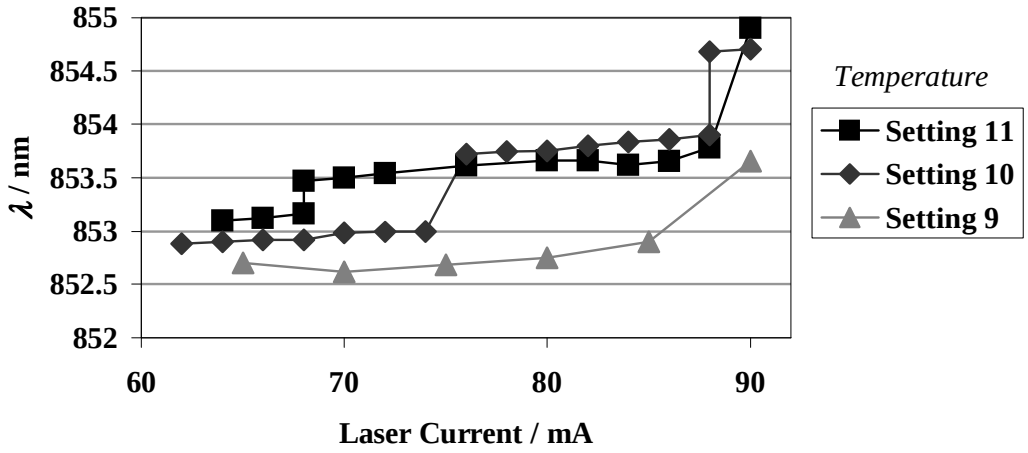

Figure 4-1: Free-Running Diode Spectrum

The tuning range of the diode can be substantially extended by the addition of an external cavity. The linewidth is simultaneously reduced with a minimal loss in the output power.[11][12] The external cavity used is described in further detail in section 4.1.4.

Two different types of semiconductor laser were used. Three Hitachi HL8318G type diodes fell victim to the back-reflected idler beam, which necessitated an increasingly complex protection layout, described in section 4.2. For the successful injection seeding results presented in this dissertation, a Sharp LT015MD0 diode was used. The two types of diode are similar and emit about 30 mW of power when driven by currents around 100 mA.

4.1.2 Temperature Control

Since the diode modes drift with changing temperature, the diode mounting block was temperature stabilized using a heating element in conjunction with a thermistor and a negative feedback loop. Although the durability of the diodes is reduced at higher temperatures, a heater was used in preference to a Peltier cooling element for simplicity. The controller was not calibrated, so the settings of the temperature adjust knob are recorded instead of absolute temperature. The temperature tuning of the diode was not exploited because of the low speed of thermal processes and because it was not necessary with the external cavity.

It was found that temperature stabilization was not required, provided there was no movement of people in the laboratory. The diode was placed inside a closed box to reduce the effect of air currents.

4.1.3 Focusing Lens

One of the greatest disadvantages of laser diodes is that their extremely narrow active region causes the output beam to be strongly divergent. This was corrected to a considerable extent by mounting a collimating lens immediately after the diode, where care was taken to position the lens centrally on the beam and perpendicular to it. The spacing between diode and lens was adjusted until the spotsize observed in the far field was minimized. Nonetheless, the beam still had a divergence of approximately 0.1 mrad.

4.1.4 External Cavity

The external cavity was formed by a diffraction grating mounted in the Littrow configuration, so that the first diffraction order was aimed back into the laser diode to provide optical feedback. Figure 4-2 shows the relative positions of the diode, the collimating lens and the diffraction grating.

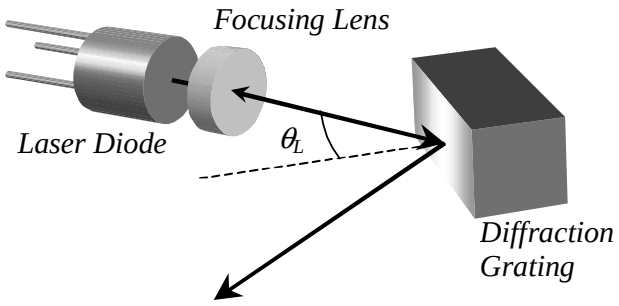

Figure 4-2: Diode Laser External Cavity

The construction used was based on a design published by Wieman *et al* in a paper aimed at atomic physics,[12] where the diffraction grating was attached to a commercial mirror mount. This arrangement was cheap and effective but had some major disadvantages. Exact alignment was a time-consuming process because the grating tilt was controlled by coarse micrometer screws, and the output of the diode laser was very sensitive to acoustic noise, both through the base plate and from the air.

The grating used had 1200 lines per mm. For a diffraction grating in the first order Littrow configuration, the angle θ_L of the beam to the normal of the grating (see Figure 4-2) is given by

$$2d\sin\theta_L = \lambda, \quad (30)$$

where d is the spacing of the diffraction lines and λ is the wavelength of the light. For our grating, the first intensity peak occurred at $\theta_L = 30.7°$.

The finite size of the diode active region and the wavelength-dependent diffraction angle of the grating combined to narrow the operating linewidth of the output. A given diode longitudinal mode could be tuned over a limited range by fine adjustment of the diffraction grating angle. These small angle changes were effected by applying a voltage to a piezo-electric element inserted between the grating mount and the horizontal adjustment screw. It is possible to obtain commercial piezo-electric transducers which change their dimensions linearly with the applied voltage, but for our purpose two piezo-electric discs soldered back to back provided a suitably controllable angle variation.

The output wavelength needed to simultaneously satisfy the selectivity of the grating and be a standing wave mode of the external cavity. Mode-hopping occurred more frequently between the external cavity modes since they were much closer together than diode longitudinal modes. Since

$$\Delta\nu_d = \frac{c}{2L_d}, \quad (31)$$

the spectral separation of the cavity modes can be increased by shortening the diode external cavity length L_d. To combat mode-hopping, the shortest possible cavity length was used, with $L_d \approx 20$ mm. Hence external cavity modes were separated by $\Delta\nu_d \approx 7$ GHz.

The output of the diode laser was the reflection off the diffraction grating, as shown in Figure 4-2. Since the grating moves when the emission wavelength of the diode is scanned, the output also moved. In practice, this effect was not significant because the beam displacement was small compared to the beam diameter, but similar diode systems used elsewhere in the Department have eliminated this beam motion by using a reflection off a beam splitter inserted into the cavity as the output. The disadvantages of this method are that diode power is lost to spurious reflections and that the cavity length needs to be increased to fit the extra optical element. These effects were both undesirable for this project, because the maximum achievable seed power and scan range were required. A final consideration when inserting the diffraction grating was to ensure that its blaze angle is oriented for the output of the cavity, which increased the output power.

4.1.5 Stability

Real-time analysis of the seed beam étalon fringes clearly indicated that the cavity was very sensitive to acoustic noise. A loud noise in the laboratory was sufficient to blur the usually sharp fringes, although no quantitative investigation was performed. The passive instability of the system could potentially be a limiting factor of successful injection seed-

ing, although this was not the case in this project. Nonetheless, preparations have begun for building a superior design for the external cavity, described by Ricci *et al.*[11] The system is commercially available from a company specializing in diode laser systems but is prohibitively expensive. Suitable material comprising high heat conductivity, low heat capacity and high elasticity was found and will be used to construct such a system in the future.

4.2 Configuration

The junction regions of diode lasers can very easily be destroyed by high intensity light entering the diode. Under usual working conditions this is not a problem, since scattered light is too weak to affect the semiconductor, but the extremely short duration of the pulses involved in the experiments meant that even beams with very low average power had enough peak intensity to destroy the diode.

Injection seeding in collinear operation requires that the pump, signal, idler and seed beams all follow the same path through the OPO. The basic configuration is for the signal and idler beams to exit the OPO from the end opposite to where the pump enters. Although the cavity mirrors were chosen for single resonance at the signal wavelength (see Appendix C), it was found that such a simple configuration was imperfect since back-reflections of beams in the cavity had sufficient energy to destroy the diode laser. Depending on the circumstances, the damaged diode would either fail to emit any light at all or no longer lase but still operate as an LED. Several diodes were damaged in the development of the protection layout described below.

4.2.1 Beam Dispersion

In the simple configuration with the diode laser pointing directly along the axis of the OPO, it was the pump and signal beams which were most likely to be responsible for damaging the diode.

The pump was the most conceivable, being the one with the highest peak energy. The cavity mirrors were chosen for high transmission at the pump wavelength, but there were weak reflections from the output coupler due to the refractive index step at the mirror substrate. The reflection coefficient for these Fresnel reflections obeys

$$R = \frac{(n-1)^2}{(n+1)^2}, \quad (32)$$

which for the $n = 1.5$ fused silica mirrors of the cavity corresponded to $R = 4\%$. The cavity mirrors were aligned to be exactly perpendicular to the pump beam (see Appendix B.1) so

the reflected beam travelled directly to the diode. Fresnel reflections also occurred at the crystal faces, but since the OPO wavelength was adjusted by rotating the crystal with respect to the pump beam it was clear that in general the reflections would not be aligned with the arriving pump. It was observed in the laboratory that the reflections deviated in the vertical as well as the horizontal plane, indicating that the crystal faces were not cut exactly perpendicular to its edges.

It was also possible that the laser diode was destroyed by a signal pulse, since the signal was travelling towards the diode inside the OPO cavity as it was resonated. When the seeding experiment was first set up, the input mirror of the OPO was a 95% signal reflector, so a significant amount of signal leaked through this mirror to the diode.

Since both the pump and signal beams had a substantially different wavelength to the seed, the easiest way to eliminate their back-reflections was to arrange a dispersive element and a long path length between the OPO cavity and the seed laser. A prism was used in preference to a diffraction grating because it had lower losses at the low intensity infrared wavelengths of the seed. The prism was aligned using the seed beam, i.e. by ensuring that the seed travelled through the OPO after passing the prism. In the arrangement used, the total path length between the laser diode and the prism measured 5.3 m, although it was observed that the pump and signal beams deviated about 1 cm/m from the seed, so a shorter path length and appropriate aperturing should be sufficient.

4.2.2 Faraday Isolator

Despite the fact that the pump and signal beams clearly did not reach the diode, careful alignment of the seed to the pump still caused the destruction of the seed laser. This implied that the peak intensity of the Fresnel reflection of the idler off the output coupler was sufficient to damage the diode. It was observed that the reflected idler was intense enough at the diode to be seen with an IR viewer but too weak to be detected by a power meter.

When the OPO was seeded, the seed and idler beams followed exactly the same path and had the same wavelength, the only difference between them being the direction in which they are travelling. In order to severely attenuate the reflected idler, a large-aperture tunable Isowave I-80-T4M Faraday isolator was inserted between the diode and the OPO, which had a specified insertion loss of no more than 0.4 dB and a typical attenuation of ≥ 40 dB in the reverse direction.

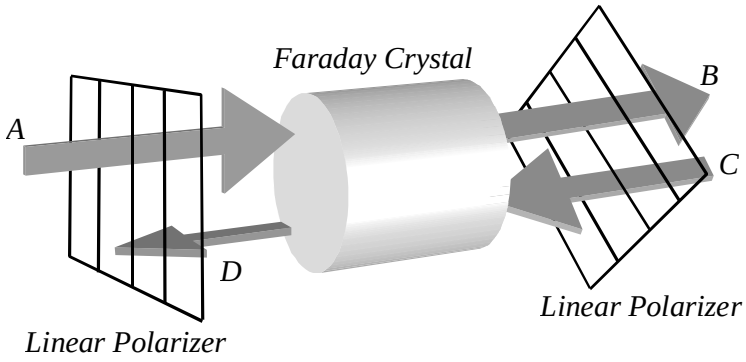

Figure 4-3: Faraday Effect

The Faraday effect (Figure 4-3) occurs in certain materials when a strong magnetic field is applied. It rotates the plane of polarization in opposite directions relative to the beam propagation for counter-propagating beams. In our case, vertically polarized light from the diode laser (*A*) was rotated through 45° by the crystal and transmitted by a second linear polarizer (*B*). The reverse-travelling idler beam (*C*) entered with the same 45° polarization but was rotated oppositely to the seed, so its horizontal polarization was blocked by the first polarizer (*D*).

The Isowave isolator used was tunable over 750-900 nm by variation of the angle between the polarizers. When optimized for the 854 nm wavelength of the seed beam, the measured attenuation in the reverse direction was almost 41 dB. Exact alignment was very difficult and the attenuation very sensitive to slight changes in angle between the polarizers.

4.2.3 Half-Wave Plate

After passing through the Faraday isolator, the plane of the seed polarization was at 45° to the vertical axis. Injection seeding requires matching polarizations of the seed and idler beams in the nonlinear crystal, so a half-wave plate was inserted after the isolator to restore the seed to vertical polarization. A half-wave plate consists of an anisotropic crystal which retards the polarization component along a particular axis. By changing the angle between this axis and the plane of polarization of the light, the direction of polarization can be altered by an arbitrary amount. Since the half-wave plate is not propagation direction sensitive, it could not be used on its own to eliminate the reflected idler from the seed beam.

4.3 Diode Laser Results

Progress in obtaining the largest possible single mode scan range was hindered by the large number of variables requiring adjustment. These variables included diode temperature,

diffraction grating alignment, and the relationship between the piezo-electric disc voltage ramp and the simultaneous current ramp.

4.3.1 Diode Temperature

An arbitrary temperature setting of 10 was originally chosen but was later changed to half-way between settings 10 and 11 because no amount of peaking of the other parameters provided an acceptable scan range.

4.3.2 Diffraction Grating Alignment

The grating was coarsely aligned by projecting the output beam to a distant wall and raising the injection current significantly above threshold. Two separate beams were observed; the laser output reflected off the grating and a weaker reflection of the first diffraction order off the front face of the diode chip. By tilting the grating, these beams were made to coincide. The current was then reduced to threshold, where the intensity of the beam became rapidly dim. The intensity of the output beam was observed to flash brightly as the vertical alignment was changed (Figure 4-4). By iteratively minimizing the threshold current, the vertical tilt was optimized. The scan range of the external cavity was found to be extremely sensitive to this angle. Near threshold, changing the horizontal angle also caused the intensity of the output to flash, but there were a large number of peaks under a general envelope. This intensity distribution is also sketched in Figure 4-4. The horizontal angle was chosen to be near the centre of the envelope and on one of the bright fringes, thus further reducing the threshold current.

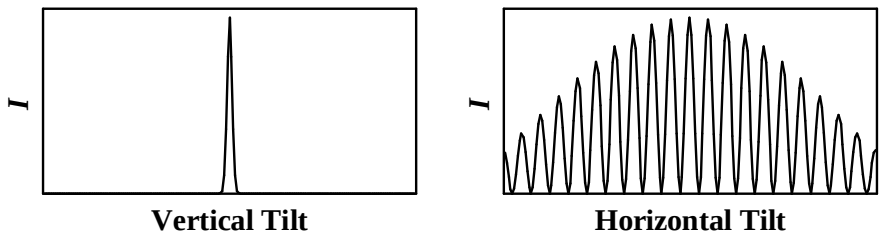

Figure 4-4: Beam Intensity with Grating Alignment (Sketch)

Careful alignment of the grating reduced the laser diode threshold current from 37 mA to 30.3 mA. This agreed with the published ≈15% reduction in threshold current expected for well-aligned external cavities.[11] By comparing the measured wavelength before and after the diffraction grating is added, it was found that the external cavity was operating at almost the same wavelength as the free running diode. Throughout the seeding experiments, the

diode output was measured to lie between 853.7 and 854.2 nm, agreement with the free-running wavelength shown in Figure 4-1.

4.3.3 Injection Current and Piezo-Electric Disc Voltage

The movement of the diode laser fringes from a 20 mm étalon was observed as the injection current and the piezo-electric voltage were varied. The results are sketched in Figure 4-5. The vertical axes are intended as a guide only; the exact currents and voltages where the diode operated in single mode depended on the other parameters.

It was found that the diode output changed from single mode, with a linewidth below the resolution of the étalon, to a structureless region in regular intervals. The change was consistently smooth or discontinuous at a particular boundary, as shown. During the smooth change from single mode to blur, two subsidiary modes would appear beside the main peak before all structure was lost.

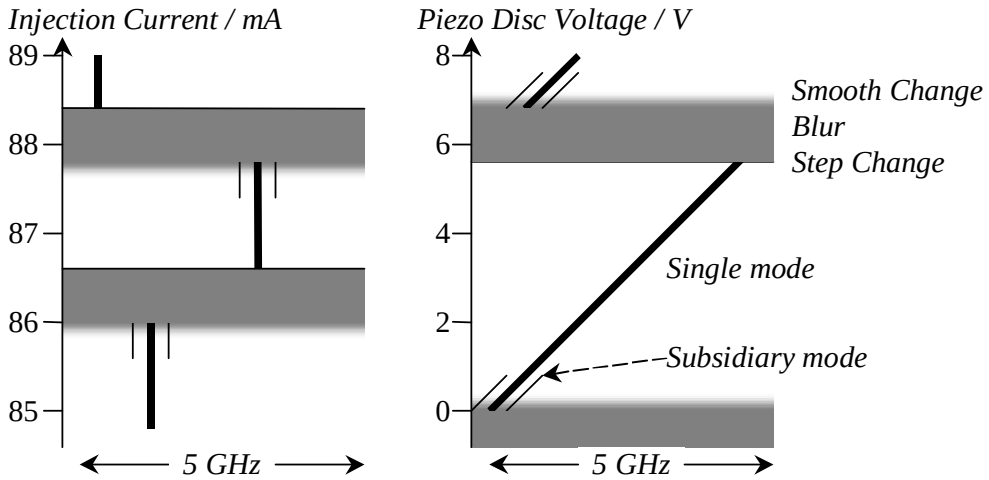

Figure 4-5: Structure of Diode Laser Output (Sketch)

Slices through the pattern generated by the 20 mm étalon are shown in Figure 4-6. The centre of the interference pattern is visible at the right of the graphs. The top panel shows the single mode of the diode. In the second graph, the subsidiary modes have appeared and in the third almost all structure has been lost.

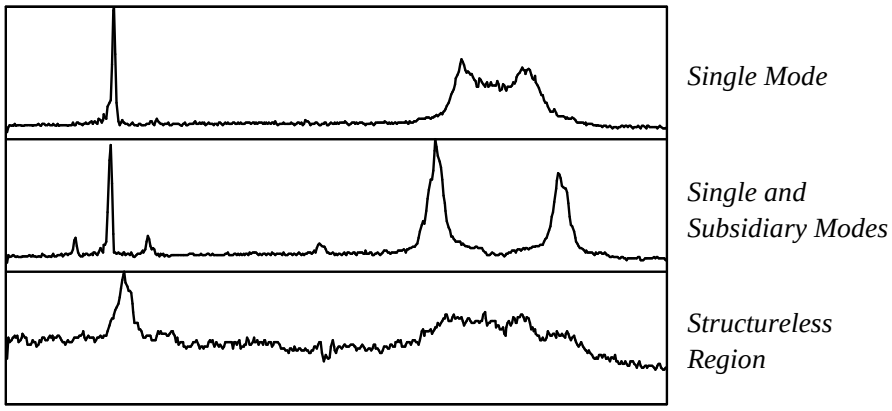

Figure 4-6: Diode Mode Structure through 5 GHz Étalon

To investigate this effect further, the single and blurred modes of the diode were passed through the étalon with the largest FSR available. Figure 4-7 shows the two regions of operation as viewed through the 100 GHz étalon. Since there is no structure visible on this scale, this would indicate that the diode is operating at multiple longitudinal or transverse modes.

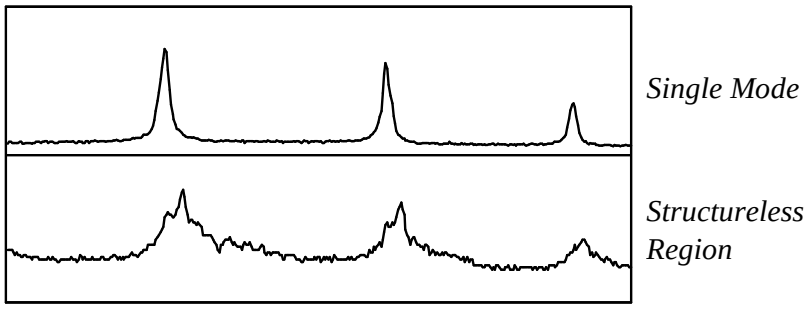

Figure 4-7: Diode Mode Structure through 100 GHz Etalon

4.3.4 Single Mode Scan

The blurred emission phenomenon discussed above was not investigated further because it was found that it did not affect the single mode scan range possible. With the laser parameters optimised, the voltage to the piezo discs and the injection current to the diode were simultaneously scanned. Although Figure 4-5 shows that scanning the diode current does not systematically change the emission frequency, the synchronized scan caused the gain envelope of the diode to track the changing wavelength selectivity of the diffraction grating. A 19 GHz single mode scan was obtained, which is comparable to the best published results using similar external cavity systems.[11]

If the relative amplitudes of the current and voltage ramps were not adjusted correctly, then the scan range obtained was reduced because mode hopping occurred. Even when very

carefully matched, slight changes in operating conditions such as temperature drifts introduced the subsidiary modes shown in Figure 4-5. A minor change to the laser current eliminated these modes.

A series of strips through the 7 mm étalon fringe pattern is shown in Figure 4-8. The increasing width of the peaks toward the right edge of the graph is an artefact of the scaled *x*-axis to linearize the fringes. The arrow indicates the direction in which the single mode travels. This scan was reproducible at a variety of initial currents and offset voltages. A carefully chosen pair of starting conditions would allow the diode to be scanned in single mode over the entire range available from the piezo-disc voltage supply.

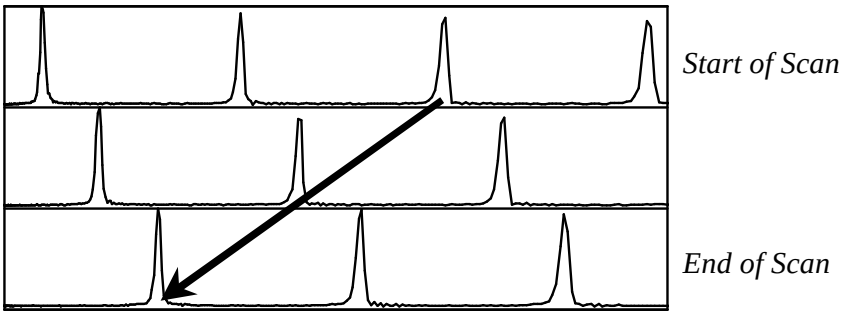

Figure 4-8: Single Mode Scan through 14 GHz Etalon

4.4 Injection Seeding Results

The table arrangement shown in Figure 3-6 provided poor seeding. It was thought that the principal reason for this was the weak seed beam intensity at the OPO. The extended beam path and numerous components caused the beam diameter to exceed the dimensions of the crystal and reduced the seed intensity to below 1.5 mW at the OPO cavity. To obtain successful seeding, the seed configuration was modified.

4.4.1 Experimental Modifications

The simplest modification of adding a long focal length lens after the prism did not seem to significantly affect the success of the seeding process. It was thought that this was because the seed beam was still larger than the pump beam at the OPO, since the lens was so distant from the cavity. The lens could not be inserted closer to the cavity since the pump beam was coincident with the seed there. For successful seeding, the seed needs only to cover the same volume of the crystal as the pump does, since regions outside the pump beam do not experience the nonlinear gain. To provide more flexibility for focusing optics, the pump beam path was modified as shown in Figure 4-9.

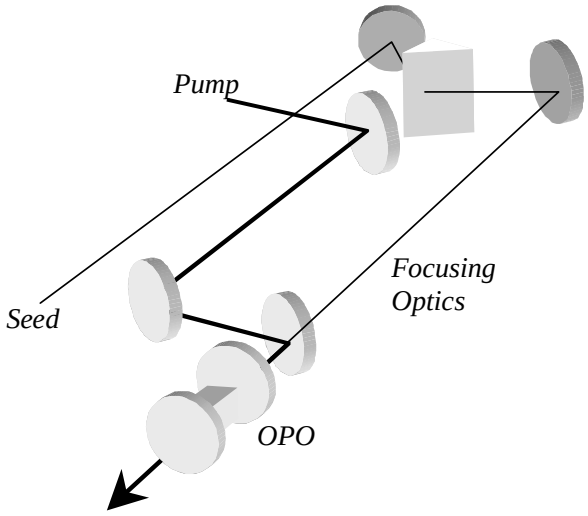

Figure 4-9: Modified Beam Paths

A single lens as close as possible to the OPO in the region marked focusing optics allowed the seed beam to be focused to an extremely narrow waist. This permitted seeding to occur more readily, but not consistently. Seeding was enhanced by placing a ×2.5 telescope in reverse in the region marked focusing optics. This narrowed the seed beam waist such that clipping by the crystal did not occur and kept the divergence of the beam to a minimum. The seeding results presented in the next section were obtained using the telescope configuration. The telescope and lenses had the added advantage that they caused idler divergence and therefore reduced its intensity.

4.4.2 Seeding Results

A progression of seeding results is shown in Figure 4-10. In each case, the left panel gives a slice through the image produced by the 20 mm étalon, with the vertical line indicating the centre of the interference pattern. The *x*-axis of the graphs has been linearized such that successive interference peaks occur at equal intervals. The relative height of the peaks is of no importance. The decaying amplitude is caused by the decreasing illumination of that part of the pattern. At the right is a lineshape profile of the same seeding obtained by scanning the spectrometer. The full width of the right-hand graphs is 10 nm, with all but the first graph centred on the seed wavelength of 854.1 nm. $\Delta\lambda$ in this case refers to the deviation of the wavelength to the seed. The vertical axes of the graphs have been normalized.

Panel *A* shows the unseeded OPO output for comparison to the seeding results. The linewidth from the right-hand graph is of the order of 2 nm. Panels *B* and *C* show seeding on modes nearer to the centre of the free-running gain profile. From the left-hand graphs it can be seen that seeding was more successful in *B* than in *C*, which could have been due to drifts

in the OPO. Finally, panel *D* shows successful seeding at the centre of the OPO lineshape. It is this mode that we wish to use when attempting to seed while scanning the OPO.

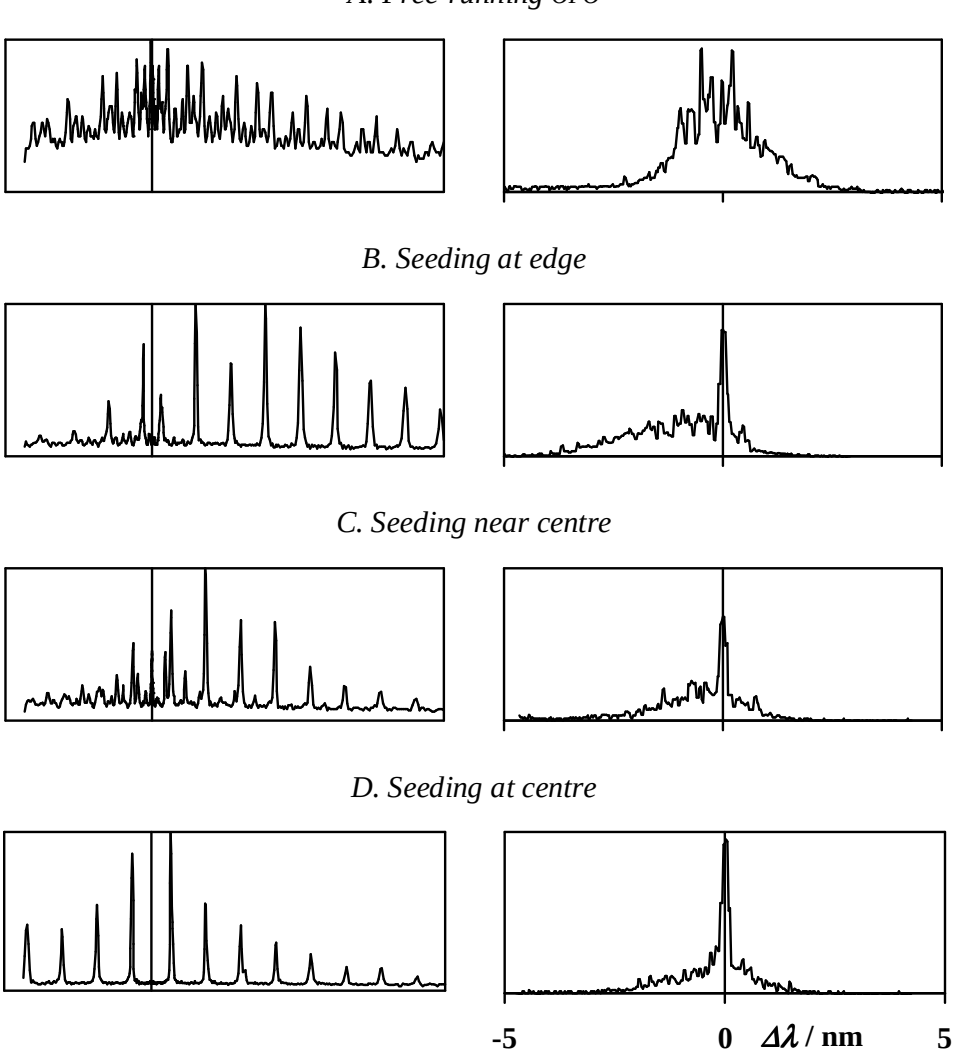

Figure 4-10: Seeding Approaching Centre of Lineshape

From the right-hand graphs in Figure 4-10, it is clear that the seeding was not completely successful, since some of the original wide lineshape can still be seen around the seeded mode. It has been revealed[22] that some published results present data from a restricted area of the seeded beam whereas results presented here involved the entire OPO output. The most obvious reason for the lack of good seeding is that the seed beam intensity was not sufficient to obtain optimal seeding. Boon-Engering *et al*, who used an arrangement very similar to ours except that their OPO was a ring cavity, reported a minimum seed power of 1 mW inside the cavity, which is close to the maximum power available to us. This proposition is also supported by the graphs shown in Figure 4-11, which show decreasing effectiveness of

the seed process as the seed intensity is further reduced by neutral-density filters. The graphs are comparable to those in Figure 4-10, showing a width of 10 nm centred on the seed wavelength.

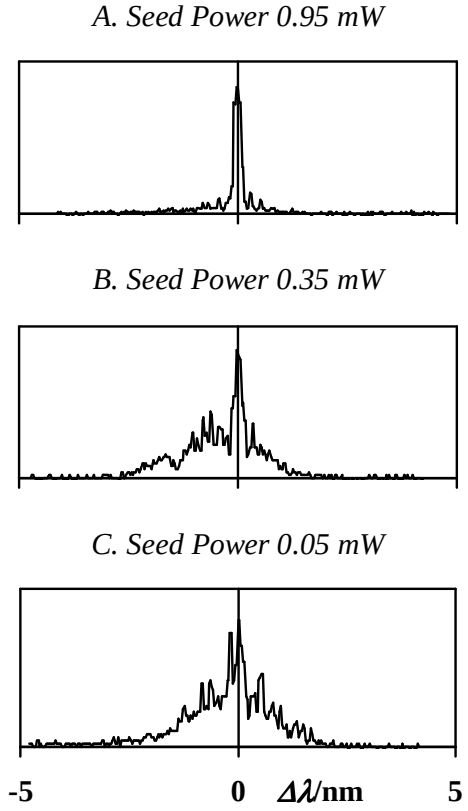

Figure 4-11: Effect of Seed Power on Seeding

However, seeding was in some cases observed on the subsidiary modes. Figure 4-12 shows strips of the seed laser and corresponding seeded idler through a 7 mm étalon. It was observed that scanning the diode through about 7 GHz allowed the same OPO mode to be seeded by the main mode and then the subsidiary mode. This implied that the secondary modes are the adjacent external cavity longitudinal modes of the diode laser.

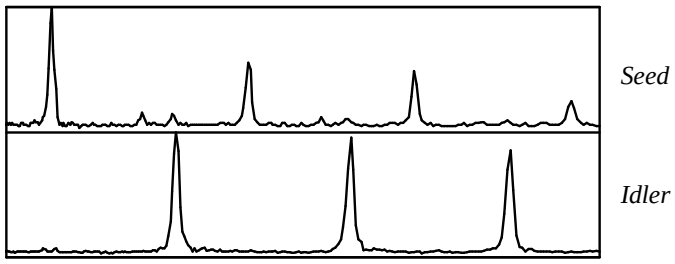

Figure 4-12: Seeding on Subsidiary Mode through 14 GHz Etalon

4.4.3 Scanned Seeding

The ultimate aim of this project was to continuously seed the OPO while its wavelength is scanned. The intention was to vary the signal frequency by changing the thermistor set-point voltage in. Since the signal is resonated in the cavity, it must be a standing wave with its wavelength λ_1 satisfying

$$\frac{m\lambda_1}{2} = L \text{ , (33)}$$

where m is an integer and L is the optical cavity length given by

$$L = L' + (n_o - 1)l. \text{ (34)}$$

Here L' and l are the physical lengths of the cavity and nonlinear crystal respectively. We use n_o in equation (34) because the signal is an ordinary beam. The refractive index n_o is a function of the temperature T of the crystal, which is in turn a function of the thermistor set-point voltage V supplied by the ramp generator. Hence the signal frequency as ν_1 could be expressed as $\nu_1(V)$ but since we are only interested in a scan $\Delta\nu_1$ we use differential calculus to obtain the expression

$$\begin{aligned}\Delta\nu_1 &= \frac{\partial\nu_1}{\partial\lambda_1}\frac{\partial\lambda_1}{\partial L}\frac{\partial L}{\partial n_o}\frac{\partial n_o}{\partial T}\frac{\partial T}{\partial V}\Delta V \\ &= -\frac{mcl}{2L^2}\frac{dn_o}{dT}\frac{dT}{dV}\Delta V.\end{aligned} \quad (35)$$

Using values l = 12 mm, L = 26 mm, $m \approx 86000$, $dn_o/dT = -16.6\times10^{-6}$ K^{-1}, and $dT/dV \approx$ 50 KV^{-1}, we obtain

$$\frac{d\nu}{dV} = 95 \text{ GHz/V. (36)}$$

The OPO temperature ramping electronics were limited to a scan of about 0.1 V near the centre of the temperature curve of Figure 3-3. We therefore expect factors other than the diode laser range to limit the scan length.

The limited unscanned seeding success prevented a lengthy investigation into the scanned seeding process. It is thought that in a more stable seeding environment scanned seeding might be achieved in the near future.

Chapter 5 Threshold

5.1 Model

There have been a number of numerical models reported for the operation of OPOs. The model used in this dissertation was published in 1979 by Brosnan and Byer.[7] Since then there have been numerous improved models accounting for effects such as injection seeding.[15] The recent increase in available computing power has enabled models to predict temporal series and fluence profiles,[14] and allow for tracking of multiple modes through the cavity to investigate the phenomenon of gain competition between modes.[10]

The model presented by Brosnan and Byer uses an iterative solution but can be simplified to yield a direct analytical expression by making suitable assumptions. We proceed from equation (26) by assuming that the time profile of the incident pump is Gaussian, such that the net gain of the cavity obeys

$$\Gamma = \Gamma_0 \, e^{-(t/\tau)^2}. \quad (37)$$

Here τ is the $1/e^2$ intensity half-width of the pump. The signal power for pass m can then be found to be

$$P_m = P_{m-1}\left(Re^{-4\alpha l}\cosh^2\left[\Gamma_0 e^{-(t_m/\tau)^2} L\right]\right), \quad (38)$$

where the pump intensity is assumed to be constant during one round trip. R is the reflection of the output coupler. The intensity of the signal at threshold is defined to be 100 μJ, which yields a threshold power to noise ratio of $\ln(P_n/P_0) = 33$. Equation (38) is iterated for a given pump amplitude Γ_0 and the threshold pump energy is found when the signal intensity at the end of the net gain period inside the oscillator is above the defined threshold signal intensity level.

This model is simplified by replacing Γ with a time-independent gain profile, the width of which is given by the time over which the oscillator has net instantaneous gain. The height is found by requiring that the total gain of the time-independent profile matches that of the Gaussian one. A final simplification assumes that the time over which there is net instantaneous gain is 2τ, which is approximately true for most oscillators.

We obtain a relation of the form

$$J_0 = \frac{2.25}{\kappa g_s L^2}\tau\left[\frac{L}{2\pi c}\ln\frac{P_n}{P_0} + 2\alpha l + \ln\frac{1}{\sqrt{R}} + \ln 2\right]^2 \quad (39)$$

for the threshold fluence. Here

$$\kappa = \frac{2\omega_1\omega_2 d_{eff}^2}{n_1 n_2 n_3 \varepsilon_0 c^3}, \quad (40)$$

where the n_i are the refractive indices for the signal, idler and pump respectively. The remaining symbols are defined in equations (12), (17), (24), (25) and (38).

5.2 Values Used

In order to check the model, predictions were compared with those published previously[18] using the parameters of that OPO. Agreement was obtained to within the uncertainties in Fresnel reflectivities and published values of the nonlinear coefficients.

It is useful to summarize all the parameters and the values used in a single table. A signal wavelength of 580 nm was arbitrarily chosen for the experiments, with the only consideration being that all the cavity mirrors available should resonate this wavelength.

Parameter	*Symbol*	*Value*
Nonlinear Coefficient	d_{eff}	2.02 pmV^{-1}
Absorption Coefficient	α	0.01 cm^{-1}
Walk-off Angle	ρ	4.132°
Optical Cavity Length	L	26.5 mm
Physical Crystal Length	l	12.0 mm
$1/e^2$ Pump Pulse Half-width	τ	6.795 ns
Wavelength of Signal	λ_1	580 nm
Wavelength of Idler	λ_2	915 nm
Frequency of Signal	ν_1	5.1688×10^{14} Hz
Frequency of Idler	ν_2	3.2760×10^{14} Hz
Refractive Index of Signal	n_1	1.6704
Refractive Index of Idler	n_2	1.6576
Refractive Index of Pump	n_3	1.4396
Threshold Signal to Noise Ratio	$\ln\frac{P_m}{P_0}$	33
Reflection Losses	R	0.8069
Signal Spotsize	w_1	0.425 mm
Pump Spotsize	w_3	1.27 mm

Table 5-1: Parameters for Threshold Model

Due to inconsistencies in the published values of d_{eff}, three different values[18] of 1.7 pm/V, 2.0 pm/V and 2.6 pm/V were modelled. These variations also affect the value of κ and each value is plotted as a separate line on the following graphs.

The pump pulse duration τ was converted from 8 ns FWHM from Figure 3-5 to $1/e^2$ half-width by multiplying by $\sqrt{1/2\ln 2}$. The pump beam was slightly elliptical and the pump spotsize was taken to be the shorter radius. From this, the signal spotsize was estimated such that $g_s = 0.9$, which agrees with the value in [18]. The reflection losses R take into account the four Fresnel losses of ≈4% at the faces of the BaB_2O_4 crystal per round trip. For a given output coupler reflection coefficient R_{OC}, the combined reflection losses coefficient is

$$R = (1 - 0.04)^4 R_{OC} \quad (41)$$

From Table 5-1, the following quantities may be calculated.

Parameter	*Symbol*	*Value*
Walk-off Length	l_w	16.06 mm
Gain Length	L	10.46 mm
Coupling Coefficient	g_s	0.9
Interaction Coefficient	κ	5.7370 W^{-1}

Table 5-2: Calculated Parameters for Threshold Model

To facilitate comparisons with the model, the threshold measurements obtained were converted into fluence values by assuming that the pump beam had a constant intensity across a circular region of radius w_3. All values were converted into units of Jcm^{-2}.

5.3 Output Coupling

The number of data points on the output coupler graph was limited to 4 by the number of available mirrors. The transmission profiles of these are documented in Appendix C.

Figure 5-1 shows the threshold fluence variation with output coupler. The increasing threshold with decreasing reflectivity is due to the reduced intensity of reflected signal. This increases the effective loss of the resonator. The increasing significance of the Fresnel losses as the output coupler reflectivity approaches unity causes the curves to flatten in the high energy region.

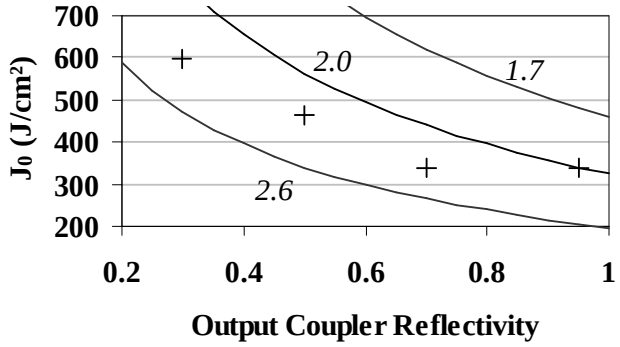

Figure 5-1: Threshold Fluence against Output Coupler Reflectivity

5.4 Spotsize

A range of different pump spotsizes were investigated by passing the beam through aluminium apertures positioned immediately before the OPO. The results are presented in Figure 5-2. In an attempt to generate uniform intensity distributions, the pump beam was first expanded using a ×2.5 telescope for apertures greater than 2 mm in diameter. The telescope was anti-reflection coated for operation at 355 nm.

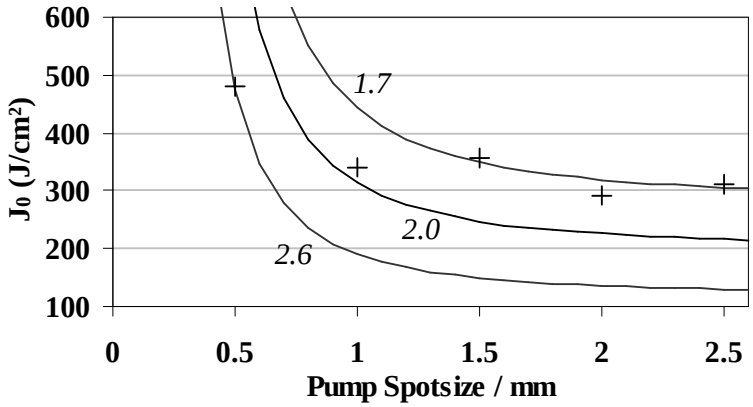

Figure 5-2: Threshold Fluence against Pump Spotsize

5.5 Cavity Length

The effect of cavity length was investigated with the 70% reflector (Figure 5-3) and with the 95% signal reflector (Figure 5-4).

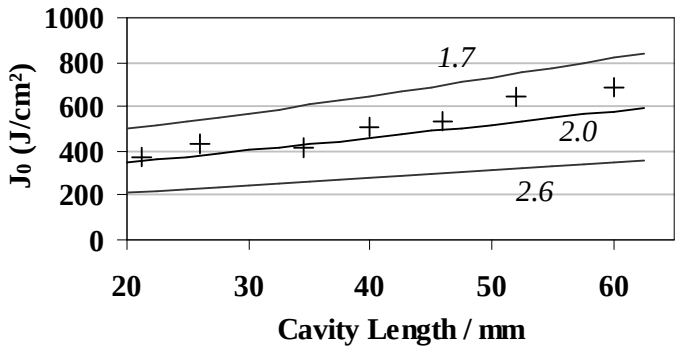

Figure 5-3: Threshold Fluence against Cavity Length, 70% R

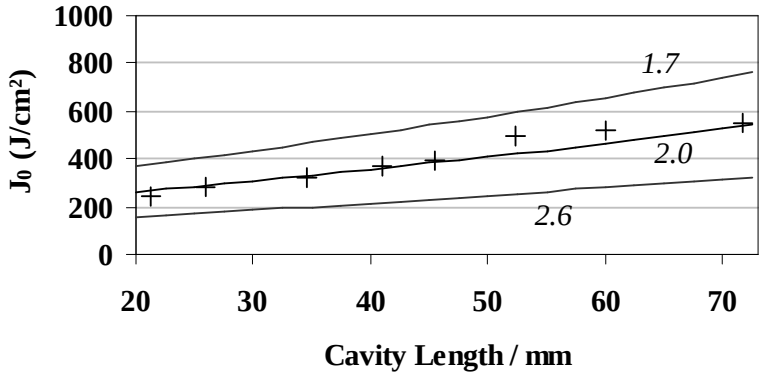

Figure 5-4: Threshold Fluence against Cavity Length, 95% R

Increasing the cavity length reduces the number of round trips of the signal during the pump pulse. Thus, to reach threshold, the signal needs to experience more gain each round trip, which causes the threshold to increase.

From the graphs it can be seen that the fixed pulse width model is in good agreement with the values obtained experimentally. The measurements indicate that the nonlinear coefficient is somewhat below 2 pm/V, but the generally higher than predicted threshold values could also be due to limitations on the measurements. Uncertainties in the cavity alignment, power meter measurements, pump spot size and difficulties in determining threshold oscillation all introduce uncertainties in the measured values.

5.6 Risetime

The risetime *t* is defined as the delay between the leading edge of the pump pulse and the onset of the signal pulse. The effects of cavity length and pump energy on the rise time *t* are shown in Figure 5-5. The trend of increasing risetime with decreasing energy is due to the lower nonlinear gain at lower pump energies, which necessitates more round-trips of the

signal before it can be detected. A longer cavity then causes the round trip time to be extended, so that increasing cavity length is associated with an increase in risetime.

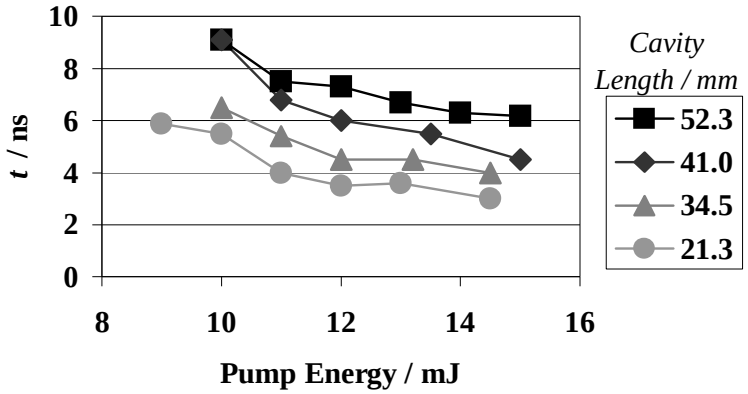

Figure 5-5: Rise Time against Pump Energy

5.7 Efficiency

Figure 5-6 shows the combined idler and signal OPO output energy E_{out} as a function of pump energy and output coupling. Over the measured pump energy range, the 70% reflector yields a higher energy. The thresholds of the 70% and 95% reflecting output couplers were experimentally indistinguishable. Higher thresholds and lower efficiencies were obtained using higher output coupling, although higher slope efficiencies would be anticipated if higher pump energies could safely be used.

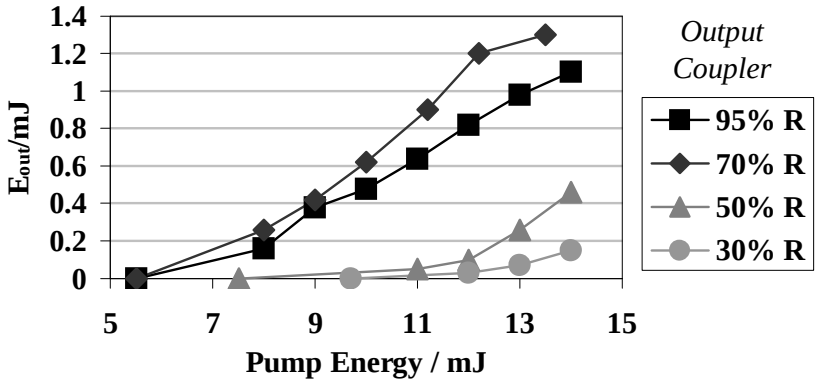

Figure 5-6: Efficiency against Pump Energy

Conclusion

The spectral properties of a semiconductor diode laser with optical feedback from an external cavity were studied. Distinct regions of single and multiple mode operation were discovered and investigated. A 19 GHz single-mode scan range was attained, comparable to the best published results for such diode systems.

The diode laser was used for successful injection seeding at the idler wavelength of a singly-resonant β-BaB_2O_4 OPO. Seeding was demonstrated at different parts of the free-running lineshape profile. The effects on seed power were investigated, and seeding on a subsidiary mode of the diode was observed.

It is envisaged that in the near future the OPO free-running envelope and the diode laser emission wavelength will be simultaneously scanned, thus providing a tunable seeded OPO. Such devices would have numerous applications in spectroscopy and atomic physics.

The effects of variations in output coupling, pump beam spotsize and cavity length on OPO threshold were measured and compared to a published model. The results agree very well to within the errors in the modelling parameters. Results of the OPO output energy and risetimes were also collected. Future modelling using this data would allow the parameters of the OPO cavity to be optimized for lowest threshold and highest efficiency.

Appendix A Diode Protection Circuit

The diode was separated from the current driver by a 2-m cable. Although the cable was shielded, the diode still needed to be protected from current spikes by a choke filter shown in Figure A-1. The circuit was constructed by Noah Russell in very constricted space at the diode end of the cable and is included for completeness.

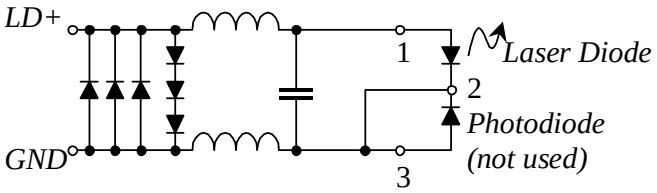

Figure A-1: Diode Protection Circuit

The photodiode shown in Figure A-1 could be used to measure the intensity emitted by the laser diode, but was not connected in the experiments presented in this dissertation.

Appendix B Alignment

Alignment is critical for the operation of the OPO, the Faraday isolator and the silica fibre. This appendix summarizes the methods used to align these devices.

B.1 OPO Cavity

The OPO cavity mirrors needed to be aligned normal to the pump beam, but since they had > 95% transmission at this frequency a separate alignment laser was used. A low power HeNe laser was chosen because the OPO cavity was resonant at visible frequencies. The HeNe was aligned with the low-power pump beam using two apertures.

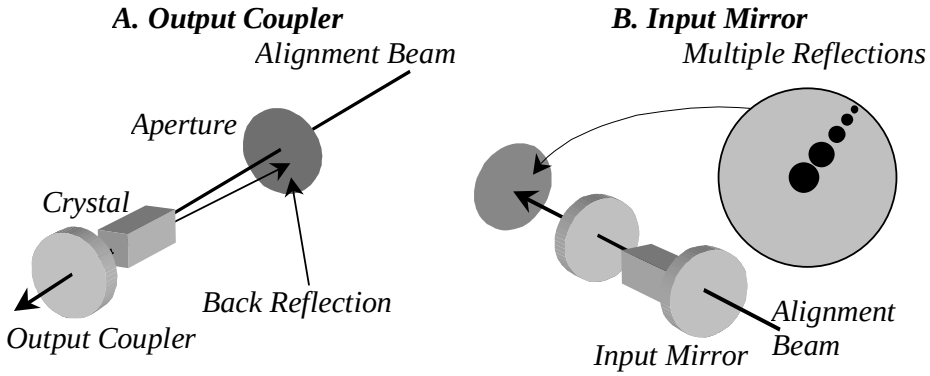

Figure B-1: OPO Cavity Alignment

The output coupler was then inserted into its mount and aligned such that the alignment laser is retro-reflected back through the aperture inserted before the OPO (*A*). There was also a second reflection, from the front face of the crystal, near this aperture (not shown).

The input mirror was then added to form the cavity. It was adjusted until the trail of multiple reflections on an aperture after the output coupler (*B*) collapsed to a single spot. The cavity then formed a Fabry-Pérot interferometer and fine adjustments were made until the centre of the fringe pattern was reached.

When the pump energy was raised, the OPO should operated in collinear mode. By reducing the pump energy to just above the threshold, final fine adjustments were made on either mirror to peak the OPO output energy.

B.2 Single Mode Fibre

Two techniques were used to align the beam into the silica fibre. The first was to centre the fibre on the beam and adjust the tilt such that the back-reflection from the focusing lens

of the fibre exactly retraced the path of the incoming beam. This alignment was made by placing an aperture on the beam and walking the reflection onto the hole.

An alternative method, preferable for weak and pulsed beams, involved placing cross-hairs on the beam before inserting the input-coupling focusing lens of the fibre. With the fibre itself removed, the lens was centred on the beam and its tilt adjusted to centre the beam after the lens on the cross-hairs. The fibre was then replaced in the mount.

Both techniques required fine-tuning, which was done while watching the output of the fibre. When the beam was properly coupled into the fibre, the output was a smooth circular disc of light.

B.3 Faraday Isolator and Half-Wave Plate

The tunable isolator needed to be carefully adjusted to the seed wavelength. The method used was to insert the isolator into the diode laser beam path in reverse and minimize its transmission. The input polarizer was matched to the diode polarization and the output adjusted for minimum transmission using a Newport Model 815 power meter.

The whole isolator was then rotated so that the seed beam was travelling in the transmitting direction. The input polarizer was again rotated to match the polarization of the seed.

The alignment of the half-wave plate was not as critical as that of the isolator, since the only adverse effect of poor alignment was a decrease in the useful seed intensity at the OPO. The half-wave plate was rotated until only vertically polarized light was observed using a Wallaston prism, which separates orthogonally polarized beams by deflection.

Appendix C Transmission Profiles

This appendix contains the transmission profiles for the cavity mirrors used throughout the experiments. The criteria for a suitable singly signal-resonant OPO cavity mirror are that it should have a high damage threshold and high (>95%) transmission at both the pump (355 nm) and idler (>700 nm) wavelengths.

Figure C-1 shows the transmission profile for the 520-620 nm high-reflector at 0° incidence. The data was obtained from the Thin Films group in the department and compares well to the specified curve. This mirror was used at the input end of the OPO.

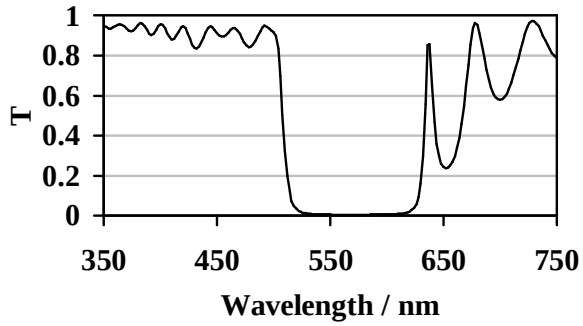

Figure C-1: Mirror Transmission for HR 520-620 nm, HT @ 355 nm

A 95% signal reflector output coupler was used for the seeding experiments (Figure C-2). During the early part of the project, a similar mirror was used at the input end, but it was later replaced by the high reflector whose transmission is shown Figure C-1.

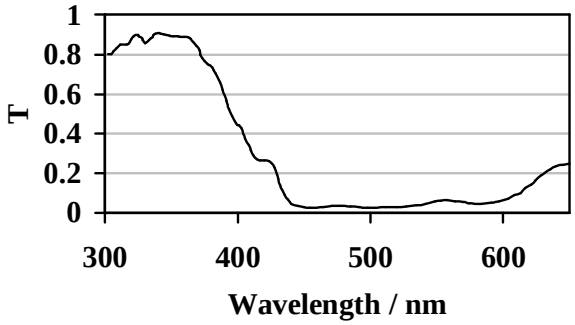

Figure C-2: Mirror Transmission for 95%R 500-600 nm, HT @ 355 nm

To investigate the effect of the output coupler on threshold level, three further mirrors were used. They were rated as 70%, 50% and 30% signal reflecting respectively, and their transmission profiles follow.

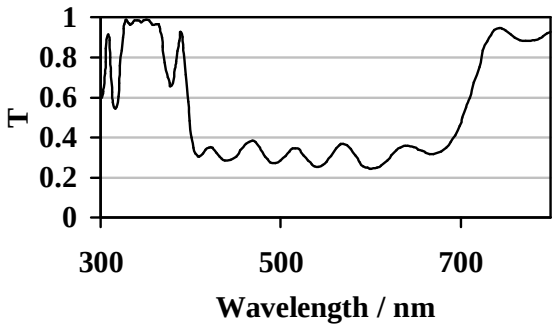

Figure C-3: Mirror Transmission for 70%R 400-700 nm, HT @ 355 nm

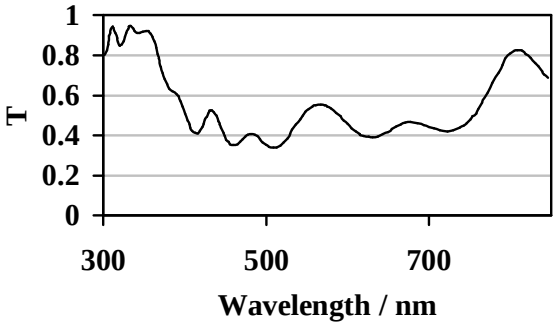

Figure C-4: Mirror Transmission for 50%R 400-700 nm, HT @ 355 nm

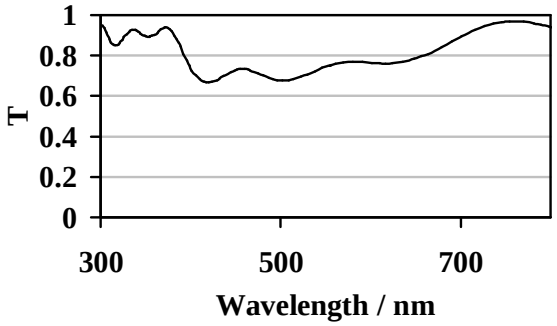

Figure C-5: Mirror Transmission for 30%R 400-600 nm, HT @ 355 nm

The graphs for the last four mirrors were digitized from manufacturer specifications, scanned to TIFF format and processed using Matlab.

References

[1] *Photonics Spectra*, pp90-91 (1995).

[2] P.A. Franken, A.E. Hill, C.W. Peters, G. Weinreich, "Generation of optical harmonics," *Phys. Rev. Lett.*, 7, p118 (1961).

[3] J.A. Giordmaine, R.C. Miller, "Tunable coherent parametric oscillation in $LiNbO_3$ at optical frequencies," *Phys. Rev. Lett.*, 14, pp973-976 (1965).

[4] V.G. Dmitriev, G.G. Gurzadyan, D.N. Nikogosyan, "Handbook of nonlinear optical crystals," *Spinger-Verlag* (1997).

[5] J.G. Haub, R.M. Hentschel, M.J. Johnson, B.J. Orr, *J. Opt. Soc. Am. B.*, **12**, pp2128-2141 (1995).

[6] L.A.W. Gloster, I.T. McKinnie, Z.X. Jiang, T.A. King, J.M. Boon-Engering, W.E. van der Veer, W. Hogervorst, *J. Opt. Soc. Am. B.*, **12**, pp2117-2121 (1995).

[7] S.J. Brosnan, R.L. Byer, "Optical parametric oscillator threshold and linewidth studies," *IEEE Journal of Quantum Electronics*, **QE-15**, pp415-431 (1979).

[8] J.E. Bjorkholm, H.G. Danielmeyer, "Frequency control of a pulsed optical parametric oscillator by radiation injection," *Applied Physics Letters*, **15**, pp171-173 (1969).

[9] N. Russell, "Critically phase matched β-barium borate optical parametric oscillator," *Honours Dissertation, University of Otago* (1996).

[10] A. Fix, R. Wallenstein, "Spectral properties of pulsed nanosecond optical parametric oscillators: experimental investigation and numerical analysis," *J. Opt. Soc. Am. B*, **13**, pp2484-2497 (1996).

[11] L. Ricci, M. Weidemüller, T. Esslinger, A. Hemmerich, C. Zimmermann, V. Vuletic, W. König, T.W. Hänsch, "A compact grating-stabilized diode laser system for atomic physics," *Optics communications*, **117**, pp541-549 (1995).

[12] K.B. MacAdam, A. Steinbach, C. Wieman, "A narrowband tunable diode laser system with grating feedback, and a saturated absorption spectrometer for Cs and Rb," *Am. J. Phys*, **60**, pp1098-1111 (1992).

[13] J.M. Boon-Engering, W.E. van der Veer, J.W. Gerritsen, "Bandwidth studies of an injection-seeded β-barium borate optical parametric oscillator," *Optics letters*, **20**, p380 (1995).

[14] A.V. Smith, W.J. Alford, T.D. Raymond, M.S. Bowers, "Comparison of a numerical model with measured performance of a seeded, nanosecond KTP optical parametric oscillator," *J. Opt. Soc. Am. B*, **12**, pp2253-2267 (1995).

[15] E.S. Cassedy, M.J. Jain, "A theoretical study of injection tuning of optical parametric oscillators," *IEEE Journal of Quantum Electronics*, **QE-15**, p1290 (1979).

[16] Y.R. Shen, "Principles of nonlinear optics," *Wiley* (1984).

[17] B.A.E. Saleh, M.C. Teich, "Fundamentals of photonics," *Wiley* (1991).

[18] L.A.W. Gloster, "Optical parametric oscillators: Noncollinear phase matching and linewidth studies in beta barium borate," *PhD Thesis, University of Manchester* (1995).

[19] F. Zernike, J.E. Midwinter, "Applied nonlinear optics," John Wiley & Sons, 1973.

[20] AM.L. Oien, I.T. McKinnie, P. Jain, N.A. Russell, D.M. Warrington, "Efficient, low-threshold collinear and noncollinear β-barium borate optical parametric oscillators," *Optics Letters*, **22**, 859-861 (1997).

[21] W. Koechner, "Solid-state laser engineering," *Springer-Verlag* (1992).

[22] M. Dunn, Private communication with I. McKinnie, *St. Andrews* (1997).